iScience

CellPress
OPEN ACCESS

Article

Pleiotropic tumor suppressive functions of PTEN missense mutations during gliomagenesis

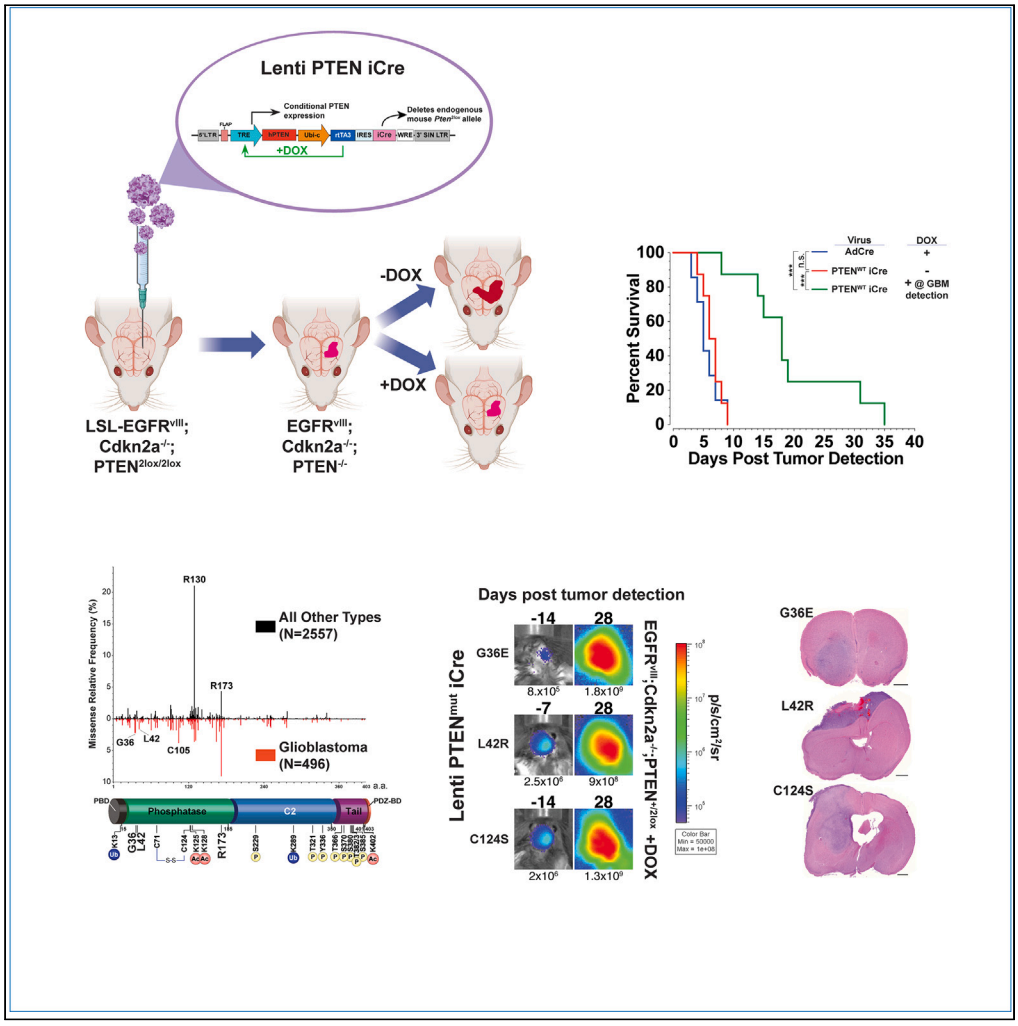

Hyun Jung Jun, Joao A. Paulo, Victoria A. Appleman, ..., Steven P. Gygi, Lloyd C. Trotman, Al Charest

acharest@bidmc.harvard.edu

Highlights

Glioma-centric missense PTEN mutants function in a dominant negative manner

Restoration of PTEN function prolongs glioblastoma survival *in vivo*

PTEN regulates EGFRvIII membrane trafficking and activity

Loss of PTEN mutants' tumor suppression parallels plasma membrane accumulation

Jun et al., iScience *27*, 111278
December 20, 2024
https://doi.org/10.1016/j.isci.2024.111278

iScience

CellPress
OPEN ACCESS

Article

Pleiotropic tumor suppressive functions of PTEN missense mutations during gliomagenesis

Hyun Jung Jun,[1,2,8] Joao A. Paulo,[3,8] Victoria A. Appleman,[1,2] Tomer M. Yaron-Barir,[4] Jared L. Johnson,[3,5] Alan T. Yeo,[1,2] Vaughn A. Rogers,[1,2] Shan Kuang,[6] Hemant Varma,[7] Steven P. Gygi,[3] Lloyd C. Trotman,[6] and Al Charest[1,2,9,*]

SUMMARY

PTEN plays a crucial role in preventing the development of glioblastoma (GBM), a severe and untreatable brain cancer. In GBM, most PTEN deficiencies are missense mutations that have not been thoroughly examined. Here, we leveraged genetically modified mice and isogenic astrocyte cell cultures to investigate the role of clinically relevant mutations (G36E, L42R, C105F, and R173H) in the development of EGFR-driven GBM. We report that the loss of tumor suppression from these mutants is unrelated to their lipid phosphatase activity and rather relate to elevated localization at the cell membrane. Moreover, expression of these PTEN mutations heightened EGFR activity by sequestering EGFR within endomembranes longer and affected its signaling behavior. Through comprehensive studies on global protein phosphorylation and kinase library analyses in cells with the G36E and L42R PTEN mutations, we identified distinct cancer-promoting pathways activated by EGFR, offering targets for treating GBM with these PTEN alterations.

INTRODUCTION

Glioblastoma (GBM) remains an untreatable cancer characterized by its rapid progression and profound resistance to existing treatments. Individuals diagnosed with GBM have a bleak outlook with an average survival time of less than 15 months. This grim situation highlights the urgent necessity for groundbreaking treatment approaches informed by a thorough comprehension of GBM's underlying biology.

The genomic landscape of GBM is well defined.[1–4] Notably, about 65% of GBM patients exhibit aberrant overexpression and activation of the epidermal growth factor receptor (EGFR) due to focal gene amplification, missense mutations, and rearrangements. In GBM, the most common EGFR mutation is an in-frame intragenic deletion of exons 2–7 that result in a ligand-independent, constitutively activated receptor called $EGFR^{vIII}$ (reviewed in[5]). Amplified and mutant EGFR is often accompanied by deletions or mutations in the INK4a/ARF (CDKN2a) locus in approximately 90% of the time, and PTEN (phosphatase and tensin homolog deleted on chromosome 10) copy number variants and mutations in roughly 65% of all GBM cases.[1–4] Our previous work modeling these mutations using genetic engineering in mice has replicated various key aspects of GBM, including its etiology, histopathology, and treatment resistance.[6–9]

PTEN is a dual-specificity protein and lipid phosphatase that functions at the plasma membrane, on cytoplasmic vesicles, and in the nucleus (reviewed in[10,11]). Its deregulation, often through aberrant posttranslational modifications or subcellular localization, is a frequent occurrence in tumorigenesis. At the plasma membrane, PTEN hydrolyzes the second messenger phosphatidylinositol 3,4,5-triphosphate (PIP3) to phosphatidylinositol 4,5-biphosphate (PIP2), antagonizing lipid kinases (PI3K)-mediated signaling events usually triggered by cell growth factor receptors. This action suppresses oncogenic PIP3-dependent signaling pathways like AKT, inhibiting cell proliferation, growth, and survival (review in[12]). In the nucleus, PTEN's import is tightly regulated by post-translational modifications of specific residues (e.g., monoubiquitination or sumoylation), where it serves as a scaffold and influences PIP3-independent functions such as genomic integrity, apoptosis, cell-cycle control, and senescence.[11,13,14] In the cytoplasm, PTEN's scaffolding function impacts the activity of inositol 1,4,5-triphosphate receptors (IP3Rs) and the activation of the tumor necrosis factor (TNF)-nuclear factor κB (NF-κB) pathway, influencing Ca^{2+}-mediated apoptosis.[15,16] PTEN's tumor suppressive functions are tightly linked to its cellular localization.

[1]Cancer Research Institute, Beth Israel Deaconess Medical Center, Boston, MA 02215, USA
[2]Department of Medicine, Harvard Medical School, Boston, MA 02215, USA
[3]Department of Cell Biology, Harvard Medical School, Boston, MA 02115, USA
[4]Columbia University Vagelos College of Physicians and Surgeons, New York, NY 10032, USA
[5]Dana-Farber Cancer Institute, Harvard Medical School, Boston, MA 02215, USA
[6]Cold Spring Harbor Laboratory, Cold Spring Harbor, NY 11724, USA
[7]Department of Pathology, Beth Israel Deaconess Medical Center, Harvard Medical School, Boston, MA 02215, USA
[8]These authors contributed equally
[9]Lead contact
*Correspondence: acharest@bidmc.harvard.edu
https://doi.org/10.1016/j.isci.2024.111278

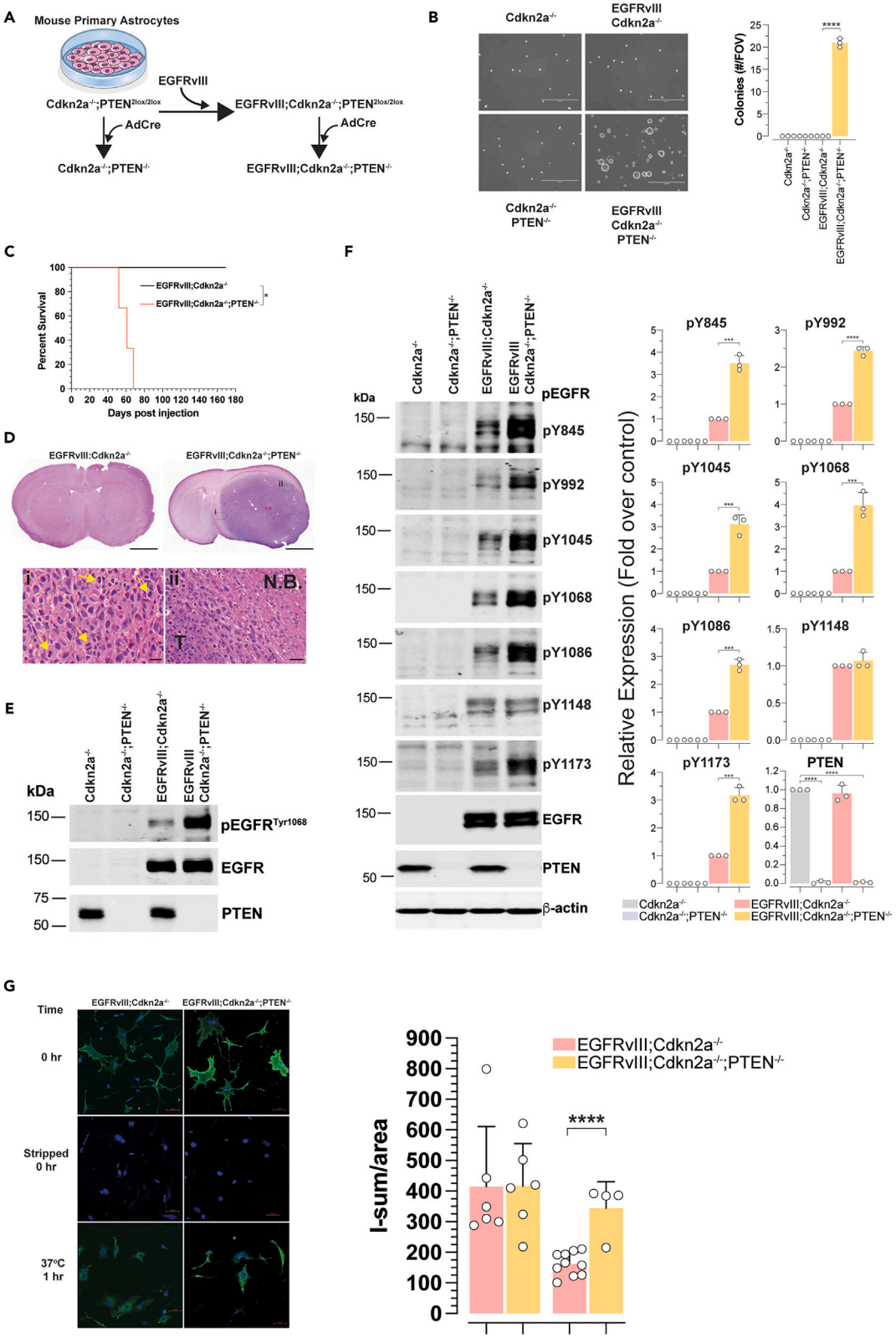
A
Mouse Primary Astrocytes
EGFRvIII
Cdkn2a-/-;PTEN2lox/2lox
EGFRvIII;Cdkn2a-/-;PTEN2lox/2lox
AdCre
AdCre
Cdkn2a-/-;PTEN-/-
EGFRvIII;Cdkn2a-/-;PTEN-/-
B
Cdkn2a-/-
EGFRvIII Cdkn2a-/-
Cdkn2a-/- PTEN-/-
EGFRvIII Cdkn2a-/- PTEN-/-
Colonies (#/FOV)
****
Cdkn2a-/-
Cdkn2a-/-;PTEN-/-
EGFRvIII;Cdkn2a-/-
EGFRvIII;Cdkn2a-/-;PTEN-/-
C
Percent Survival
EGFRvIII;Cdkn2a-/-
EGFRvIII;Cdkn2a-/-;PTEN-/-
Days post injection
D
EGFRvIII;Cdkn2a-/-
EGFRvIII;Cdkn2a-/-;PTEN-/-
i
ii
N.B.
T
E
kDa
Cdkn2a-/-
Cdkn2a-/-;PTEN-/-
EGFRvIII;Cdkn2a-/-
EGFRvIII Cdkn2a-/-;PTEN-/-
pEGFRTyr1068
EGFR
PTEN
F
kDa
pEGFR
pY845
pY992
pY1045
pY1068
pY1086
pY1148
pY1173
EGFR
PTEN
β-actin
Relative Expression (Fold over control)
pY845
pY992
pY1045
pY1068
pY1086
pY1148
pY1173
PTEN
Cdkn2a-/-
Cdkn2a-/-;PTEN-/-
EGFRvIII;Cdkn2a-/-
EGFRvIII;Cdkn2a-/-;PTEN-/-
G
Time
EGFRvIII;Cdkn2a-/-
EGFRvIII;Cdkn2a-/-;PTEN-/-
0 hr
Stripped 0 hr
37°C 1 hr
I-sum/area
EGFRvIII;Cdkn2a-/-
EGFRvIII;Cdkn2a-/-;PTEN-/-
****

Figure 1. Loss of PTEN drives EGFR^{vIII}-mediated oncogenicity in mouse astrocytes

(A) Schematic of the isogenic cell system expressing EGFR^{vIII} in the context of loss of *Cdkn2a* and conditional loss of *Pten*.

(B) Representative photomicrographs and quantification of astrocytes of the indicated genotypes grown in soft agar. Colonies >5 cells were counted from five fields of view (FOV) per biological replicate and averaged. Scale bar = 400 μm. Data are presented as the mean ± S.D. of biologically independent replicates, $n = 3$, unpaired t test, two-tailed, ****$p < 0.0001$.

(C) Kaplan-Meier analysis of orthotopic allograft of astrocytes of the indicated genotypes in immunodeficient mice ($n = 3$). *$p = 0.0246$ log rank (Mantel–Cox) test.

(D) Representative H&E-stained sections of mouse brains injected with astrocyte cultures of the indicated genotypes. Highlights of mitoses (arrows) in inset i and tumor (T) infiltration into normal brain (N.B.) inset ii are indicated. Scale bars top = 2 mm, insets i = 20 μm, ii = 40 μm.

(E) Western blot analysis of isogenic astrocyte cultures of the indicated genotypes.

(F) Representative western blot analysis (left) and quantitation (right, $n = 3$) of phospho-EGFR tyrosine residues and PTEN from isogenic astrocyte cultures of the indicated genotypes. Tyrosine residue positions are relative to the wild type EGFR sequence. Data are presented as the mean +/- S.E.M. of biologically independent replicates, unpaired t test, two-tailed, ***p<0.001 and ****p<0.0001.

(G) Representative photomicrographs (left) and quantitation (right) of indirect immunofluorescence against EGFR^{vIII} labeling plasma membrane (0 h) and endocytosed (1 h) EGFR^{vIII} signal. Scale bar = 50 μm. Data are presented as the mean ± S.E.M. of biologically independent replicates, unpaired t test, two-tailed, *$p < 0.05$, **$p < 0.01$, ***$p < 0.001$ and ****$p < 0.0001$.

Genetic analyses of PTEN germline mutation syndromes and cancer genomics studies have uncovered a wide range of PTEN missense mutations (reviewed in[17]). While some of these mutations have been thoroughly studied, the majority are still unexplored. Investigations into these mutants have been instrumental in understanding the tumor-suppressive mechanisms of PTEN. Furthermore, recent research has shed light on the functional dynamics of PTEN, particularly its ability to form dimers. This dimerization and subsequent recruitment at the plasma membrane appear to be critical for its activation and functionality.[18] In this context, the expression of missense mutation alleles of PTEN, either in the presence or absence of wild type (WT) PTEN, demands further exploration. Despite the extensive knowledge acquired so far, the functional implications of many clinically significant PTEN mutations are yet to be fully understood.

Here, we uncover functions for specific PTEN missense mutations (G36E, L42R, C105F, and R173H) that are particularly relevant to GBM. Utilizing isogenic *in vitro* and *in vivo* mouse models, we demonstrate that expression of missense mutants alters PTEN's cellular localization and activates EGFR and its signaling pathways, driving a tumorigenic program. These findings offer promising avenues for the development of therapies targeting PTEN-mutated GBMs.

RESULTS

Loss of PTEN function is required for EGFR^{vIII}-mediated cellular transformation

EGFR^{vIII} is an intragenic, in frame deletion of EGFR exons 2 to 7 that is present in approximately half of EGFR-amplified GBMs and that produces a constitutively activated, ligand-independent receptor with distinctive recycling and signaling features.[5] We previously demonstrated that modeling overexpression of EGFR^{vIII} in the CNS of genetically engineered mice along with loss of the tumor suppressor *Cdkn2a* is insufficient to generate brain tumors and that additional loss of *Pten* is necessary for tumorigenesis *in vivo*.[9] To better understand this observation mechanistically, we established isogenic primary mouse astrocyte cultures (Figure S1A) expressing human EGFR^{vIII} in the context of loss of *Cdkn2a* and conditional (Cre/*LoxP*) *Pten* deletion (Figure 1A). In these isogenic primary astrocyte cultures, complete loss of PTEN expression is conditionally achieved by infection using an adenovirus expressing Cre recombinase (+AdCre) (Figure S1B). Growth in soft agar, an *in vitro* assay of cellular transformation, was only observed in EGFR^{vIII};*Cdkn2a*$^{-/-}$;*Pten*$^{-/-}$ astrocytes and not controls (Figure 1B). When orthotopically implanted in mice, only the EGFR^{vIII};*Cdkn2a*$^{-/-}$;*Pten*$^{-/-}$ cultured cells formed lethal tumors (Figure 1C) with tumorigenic cells prominently displaying mitoses and invasive properties, which are histopathological characteristics of high-grade glioma (Figure 1D). Molecularly, we observed that loss of *Pten* in EGFR^{vIII};*Ckdn2a*$^{-/-}$ cells resulted in a noticeable increase in the level of phospho-EGFR^{vIII} on Y1068 when compared to controls, without affecting EGFR^{vIII} receptor levels (Figure 1E). Quantitative western blotting revealed that loss of *Pten* resulted in significant increases (between 3- and 4-folds over control) in the levels of all EGFR^{vIII} tyrosine autophosphorylation sites surveyed with the exception of Y1148 and no change in total levels of EGFR^{vIII} (Figure 1F). Mechanistically, we observed that loss of PTEN causes EGFR^{vIII} to internalize more efficiently and accumulate on endomembranes (Figure 1G). Together, these observations demonstrate that loss of PTEN results in heightened EGFR^{vIII} internalization concomitant with increased autophosphorylation levels and support our prior observations[9] that signaling pathways emanating from EGFR^{vIII} alone are insufficient to generate a full oncogenic response, requiring additional molecular events (in this case loss of PTEN) to drive forward an oncogenic program.

GBM-associated PTEN missense mutants trigger gliomagenesis

Analysis of large-scale, pan-cancer genomic studies[19,20] revealed that mutations of the *PTEN* gene rather than deletions are most often observed (Figure S2A) and that missense mutations represent the majority (~70%) of PTEN genomic mutations in glioma (Figure S2B). Using the COSMIC cancer genome sequencing database,[21,22] we observed that nearly every PTEN amino acid position is a target of missense mutations in cancer (Figure 2A). Notably, the frequencies of mutations at residues G36, L42, C105 and R173 differ dramatically between GBM and all other cancers (Figure 2A). These GBM-centric hotspots are found mutated to various amino acids (Figure 2A and S2C). In all cancers, the majority of PTEN missense mutations are found within the phosphatase (PTPase) domain, with R130, a site necessary for its lipid PTPase catalytic activity,[23,24] being the most prominently mutated except in GBM. A curation of COSMIC (https://cancer.sanger.ac.uk/cell_lines) and

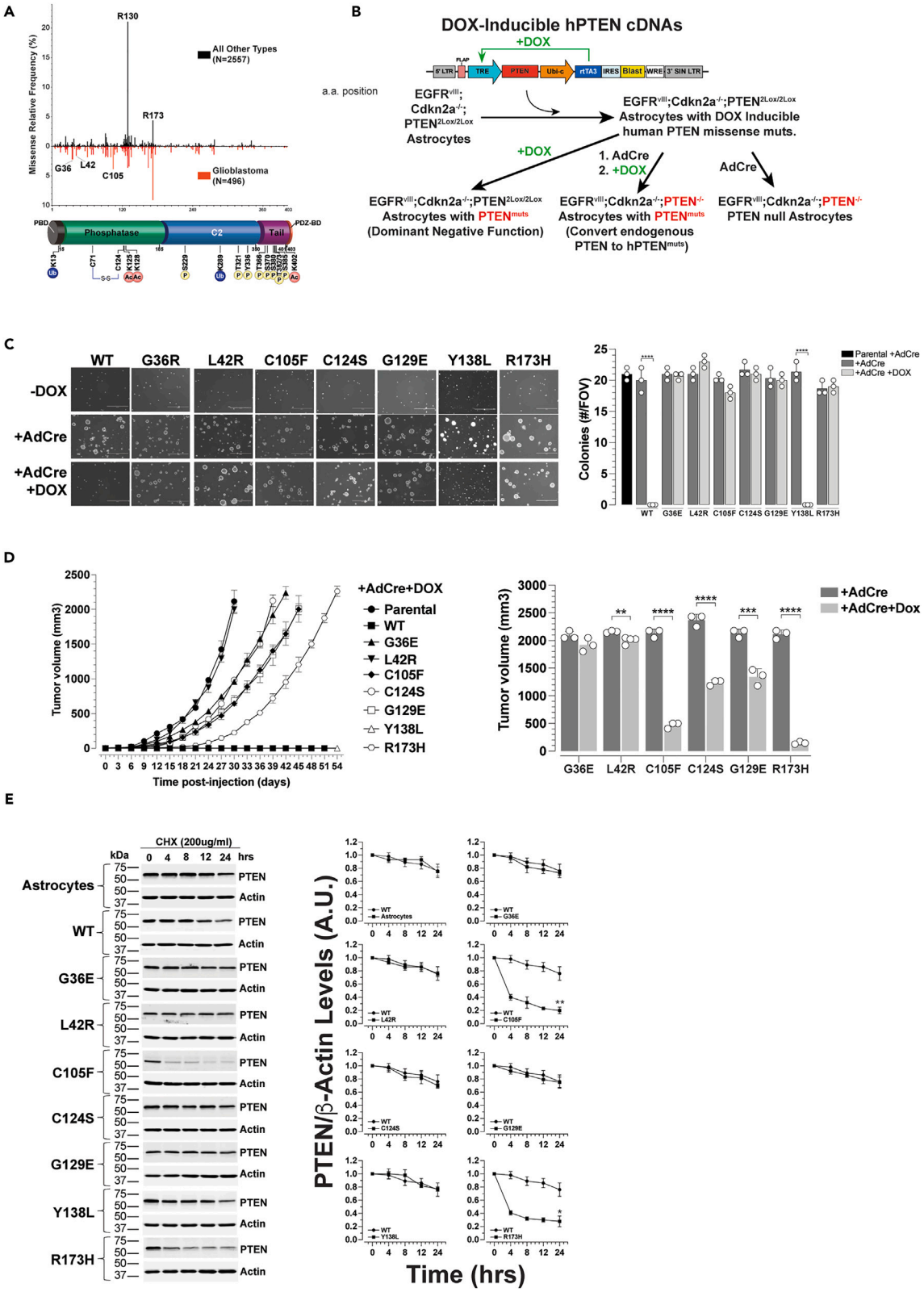
A
R130
All Other Types (N=2557)
R173
G36
L42
C105
Glioblastoma (N=496)
Missense Relative Frequency (%)
a.a. position
PBD
Phosphatase
C2
Tail
PDZ-BD
B
DOX-Inducible hPTEN cDNAs
+DOX
5' LTR
FLAP
TRE
PTEN
Ubi-c
rtTA3
IRES
Blast
WRE
3' SIN LTR
EGFRvIII; Cdkn2a-/-; PTEN2Lox/2Lox Astrocytes
EGFRvIII;Cdkn2a-/-;PTEN2Lox/2Lox Astrocytes with DOX Inducible human PTEN missense muts.
+DOX
1. AdCre
2. +DOX
AdCre
EGFRvIII;Cdkn2a-/-;PTEN2Lox/2Lox Astrocytes with PTENmuts (Dominant Negative Function)
EGFRvIII;Cdkn2a-/-;PTEN-/- Astrocytes with PTENmuts (Convert endogenous PTEN to hPTENmuts)
EGFRvIII;Cdkn2a-/-;PTEN-/- PTEN null Astrocytes
C
WT
G36R
L42R
C105F
C124S
G129E
Y138L
R173H
-DOX
+AdCre
+AdCre +DOX
Colonies (#/FOV)
Parental +AdCre
+AdCre
+AdCre +DOX
D
Tumor volume (mm3)
Time post-injection (days)
+AdCre+DOX
Parental
WT
G36E
L42R
C105F
C124S
G129E
Y138L
R173H
+AdCre
+AdCre+Dox
E
CHX (200ug/ml)
kDa
0 4 8 12 24 hrs
Astrocytes
WT
G36E
L42R
C105F
C124S
G129E
Y138L
R173H
PTEN
Actin
PTEN/β-Actin Levels (A.U.)
Time (hrs)

Figure 2. GBM-centric oncogenic PTEN missense mutants

(A) Relative frequencies of PTEN missense mutations in GBM and all other tumors compiled from Cosmic datasets mapped over PTEN's structure showing the phosphatidylinositol (PtdIns)(4,5)P2-binding domain (PBD), catalytic phosphatase domain, C2 lipid/membrane-binding domain, the carboxy-terminal tail containing PEST sequences and a class I PDZ-binding (PDZ-BD) motif. Select post translational modifications are indicated; Ac, acetylation; P, phosphorylation; and Ub, ubiquitylation.

(B) Schematic of the lentivirus vector and outline of isogenic cell generation.

(C) Representative photomicrographs and quantification of growth in soft agar assay of the indicated PTEN mutants. Colonies >5 cells were counted from five fields of view (FOV) per biological replicate and averaged. Scale bar = 400 μm. Data are presented as the mean ± S.D. of biologically independent replicates, n = 3, unpaired t test, two-tailed, ****$p < 0.0001$.

(D) Growth rates (left) and quantitation of tumor volumes (right) of subcutaneous tumors for the indicated PTEN mutant expressing $EGFR^{vIII}$;$Cdkn2a^{-/-}$ astrocytes in immunodeficient mice. Data are presented as the mean ± S.D. of biologically independent replicates, n = 3, unpaired t test, two-tailed, **p<0.01, ***p<0.001 and ****p<0.0001.

(E) Representative western blot (left) and quantitation (right, n = 3) of PTEN mutants from cultures harvested at the indicated time points post cycloheximide treatment. Data are presented as the mean ± S.E.M. of biologically independent replicates, n = 3, unpaired t test, two-tailed, *$p < 0.05$, **$p < 0.01$.

CCLE (https://sites.broadinstitute.org/ccle/) cancer cell line databases revealed 42 GBM cell lines with PTEN single nucleotide variant mutations, most of which are located within the PTPase domain (Table ST1).

To better understand the potential effects of missense mutations on PTEN's tumor suppressive functions, we isolated primary mouse astrocytes from our $EGFR^{vIII}$;$Cdkn2a^{-/-}$;$Pten^{2lox/2lox}$ genetically engineered mouse strain[6] and created isogenic astrocyte cell lines using an inducible, doxycycline (DOX)-regulated lentivirus expressing PTEN cDNAs of G36E, L42R, C105F, R173H, control wild type (WT), the dual lipid and protein phosphatase-null C124S mutant, and the lipid (G129E) and protein (Y138L) phosphatase inactive mutants[25–28] (Figure 2B). Treatment of representative clonal astrocyte populations of each PTEN missense mutant with DOX led to expression of mutant PTEN in the context of endogenous mouse PTEN protein, allowing for studies on the dominant-negative functions of these mutants (Figure 2B). Exposing these cells to AdCre deletes the endogenous mouse *Pten* gene rendering the cells null for PTEN, serving as internal control for loss of PTEN function. Subsequent treatment of the latter lines with DOX (10 μg/mL) induces expression of the human PTEN mRNAs (Figure S2D) and protein (Figure S2E) in a rapid (within 12 h) and sustained manner, as detected using qRT-PCR and western blotting. Importantly, the levels of human PTEN protein achieved are similar to endogenous mouse PTEN (Figure S2F) and higher than 95% of cells express exogenous human PTEN upon DOX induction as measured by flow cytometry (Figure S2G). Finally, DOX treatment of parental, $EGFR^{vIII}$;$Cdkn2a^{-/-}$;$Pten^{2lox/2lox}$, and $EGFR^{vIII}$;$Cdkn2a^{-/-}$;$Pten^{-/-}$ astrocytes had no measurable effects on $EGFR^{vIII}$ expression and activation nor on the signaling events downstream of $EGFR^{vIII}$ (Figure S2H).

Loss of PTEN expression (+AdCre) in all PTEN mutant and control cell cultures resulted in colony formation in soft agar with similar efficiency (Figure 2C). Induced expression (+DOX) of exogenous human PTEN mutant and control cDNAs in the latter cultures revealed that the PTEN G36E, L42R, C105F, C124S, G129E and R173H mutations promoted $EGFR^{vIII}$-driven cellular transformation whereas the Y138L mutant retained WT tumor suppressive functions (Figure 2C). Subcutaneous injection of the PTEN null (+AdCre) mutant allelic series of astrocyte cultures in mice all formed tumors at similar rates (Figure S2I). Injection of PTEN mutant (+AdCre +DOX) allelic series of astrocyte cultures in mice fed a DOX-containing diet revealed that, similar to the growth in soft agar assays, all mutants except PTEN WT and Y138L formed tumors *in vivo*, albeit with different growth rates (Figure 2D). Cells expressing C105F, C124S, G129E and R173H PTEN mutants (+AdCre +DOX) significantly grew slower than their PTEN-null isogenic counterpart (+AdCre) *in vivo* (Figures 2D and S2I). Lastly, we determined the protein stability of the GBM-centric PTEN mutations using cycloheximide treatment and western blotting. We observed that C105F and R173H PTEN mutants have significantly reduced protein stability whereas PTEN WT, G36R, L42R, Y138L, C124S, and G129E all have stabilities similar to that of endogenous mouse PTEN (Figure 2E). Together, these results demonstrate the capacity of the GBM-centric PTEN missense mutations G36E, L42R, C105F and R173H to enable an $EGFR^{vIII}$-driven oncogenic program in astrocytes leading to cellular transformation.

PTEN missense mutants accumulate at the plasma membrane and retain lipid phosphatase activity

PTEN canonically functions by antagonizing the activity of phosphatidylinositol 3-kinase (PI3K). Loss of PTEN function results in accumulation of the membrane phospholipid phosphatidylinositol (3,4,5)-triphosphate (PIP3), which activates several downstream signaling pathways. To determine whether the aforementioned PTEN mutations affect their lipid phosphatase function, we measured cellular levels of PIP3 in the PTEN mutant isogenic cells. Complete loss of endogenous mouse PTEN protein resulted in >7-fold increase in PIP3 levels while ectopic expression of human PTEN WT restored PIP3 to basal levels (Figure 3A). Ectopic expression of lipid/protein phosphatase inactive mutant C124S and lipid phosphatase inactive mutants G129E and R173H[23] failed to reduce PIP3 levels (Figure 3A). Expression of PTEN Y138L protein phosphatase mutant dephosphorylated PIP3 to basal levels, and expression of PTEN C105F partially retained PTEN lipid phosphatase function (Figure 3A). Surprisingly, expression of both G36E and L42R PTEN mutants demonstrated their full catalytic activity, reducing PIP3 to basal levels (Figure 3A). This suggests that PTEN G36E and L42R mutants cannot protect astrocytes from transformation, in spite of their full catalytic activity toward PIP3.

To evaluate the consequences of fluctuating PIP3 levels in cells expressing these various PTEN mutants, we analyzed canonical signaling pathways downstream of PTEN by western blot. Representative clonal cell populations of each PTEN missense mutant were subjected to +DOX, +AdCre, and consecutive +AdCre+DOX treatments. Similar to earlier observations (Figure 1F), loss of endogenous mouse PTEN (+AdCre) in all cultures led to substantial increases in the levels of $pEGFR^{Tyr1068}$, pan $pAKT^{Ser473}$, pan $pAKT^{Thr308}$, $pPRAS40^{Thr246}$,

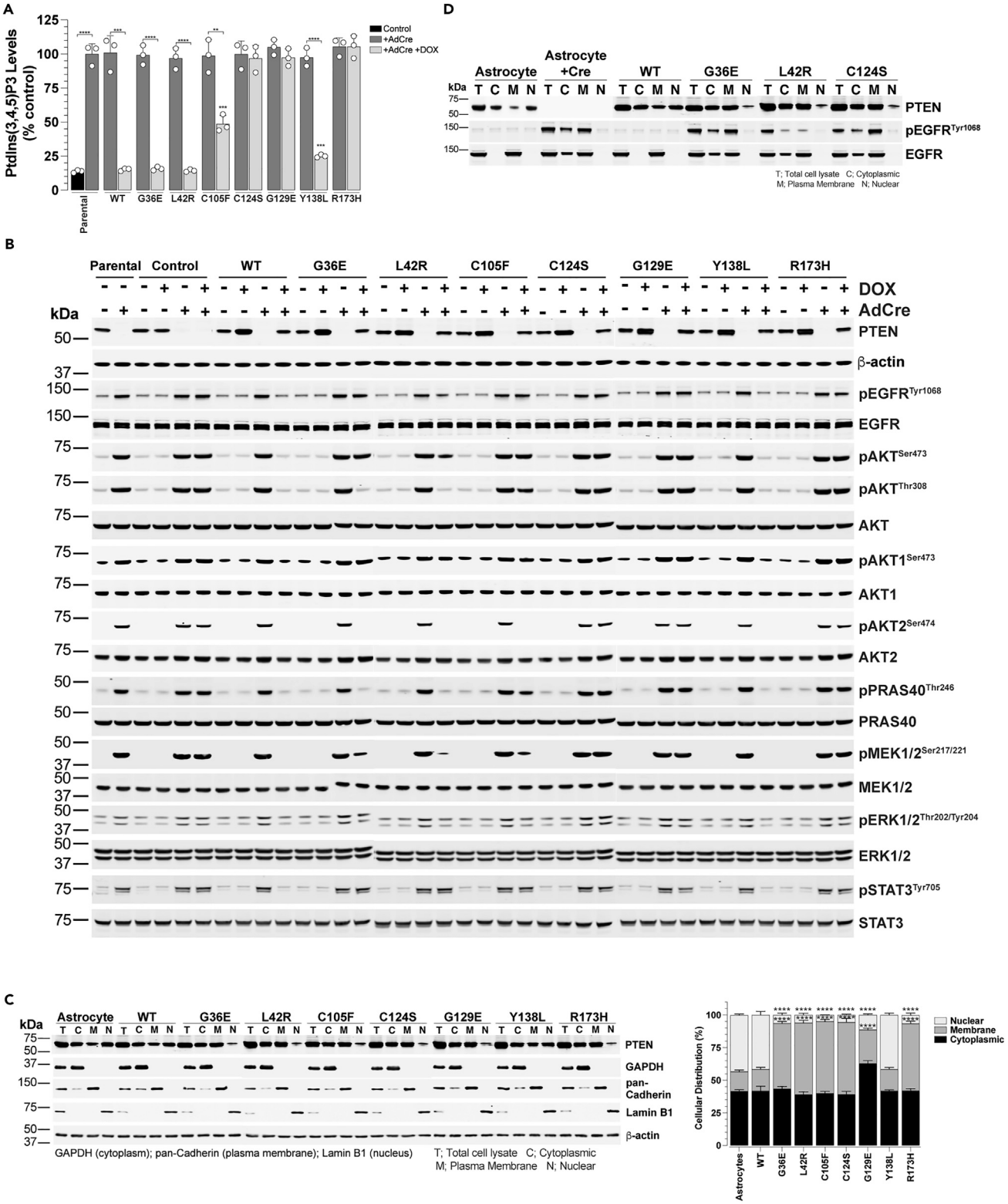
A
PtdIns(3,4,5)P3 Levels (% control)
Control
+AdCre
+AdCre +DOX
Parental
WT
G36E
L42R
C105F
C124S
G129E
Y138L
R173H
D
Astrocyte
Astrocyte +Cre
WT
G36E
L42R
C124S
T C M N
PTEN
pEGFR Tyr1068
EGFR
T; Total cell lysate C; Cytoplasmic
M; Plasma Membrane N; Nuclear
B
Parental
Control
DOX
AdCre
kDa
PTEN
β-actin
pEGFR Tyr1068
EGFR
pAKT Ser473
pAKT Thr308
AKT
pAKT1 Ser473
AKT1
pAKT2 Ser474
AKT2
pPRAS40 Thr246
PRAS40
pMEK1/2 Ser217/221
MEK1/2
pERK1/2 Thr202/Tyr204
ERK1/2
pSTAT3 Tyr705
STAT3
C
PTEN
GAPDH
pan-Cadherin
Lamin B1
β-actin
GAPDH (cytoplasm); pan-Cadherin (plasma membrane); Lamin B1 (nucleus)
T; Total cell lysate C; Cytoplasmic
M; Plasma Membrane N; Nuclear
Cellular Distribution (%)
Nuclear
Membrane
Cytoplasmic
Astrocytes

Figure 3. Enhanced plasma membrane localization and divergent signaling of PTEN missense mutants

(A) Cellular PIP3 levels in cells expressing the indicated PTEN mutants. Data are presented as the mean ± S.D. of biologically independent replicates, $n = 3$, two-tailed, unpaired t test. C105F and Y138L +ADCre+DOX are compared to PTEN WT control, $^{**}p < 0.01$, $^{***}p < 0.001$ and $^{****}p < 0.0001$.

(B) Western blot analysis of canonical signaling proteins for a panel of PTEN mutants under the indicated isogenic status.

(C) Representative western blot (left) and quantitation (right, $n = 3$) of subcellular fractions of indicated PTEN mutants. Data are presented as the mean ± S.D. of biologically independent replicates, $n = 3$, two-tailed, unpaired t test compared to PTEN WT control, $^{****}p < 0.0001$.

(D) Western blot of subcellular fractions of indicated PTEN mutants for total $EGFR^{vIII}$ and phospho-$EGFR^{vIII}$ as in (C).

pMEK1/2$^{Ser217/221}$, pERK1/2$^{Thr202/Tyr204}$ and pSTAT3^{Tyr705} (Figures 3B and S3). Using AKT isoform specific antibodies, we observed increases in levels of pAKT1^{Ser473} and pAKT2^{Ser474}, while no changes in total levels of AKT1 and AKT2 were detected (Figures 3B and S3). The elevated levels of phospho-AKT at Ser473 and Thr308 resulted in full AKT kinase activation,[12] as reflected by concomitant increases in the phosphorylation levels of PRAS40, a known substrate of AKT[29] (Figures 3B and S3). Expressing PTEN mutants G36E, L42R, C105F, C124S, G129E, and R173H in the absence of endogenous mouse PTEN (+AdCre+DOX) resulted in increases in pEGFR^{Tyr1068}, pMEK1/2$^{Ser217/221}$, pERK1/2$^{Thr202/Tyr204}$ and pSTAT3^{Tyr705} (Figures 3B and S3). Conversely, expressing PTEN WT or Y138L effectively suppressed these signaling proteins and their phosphorylation was maintained at basal levels. The PTEN G36E and L42R inhibited panAKT activation on Thr308, but not on Ser473, consistent with incomplete activation of pPRAS40^{Thr246} (Figures 3B and S3). This appears to be mainly mediated by their effect on AKT1 rather than AKT2 since only the levels of pAKT1^{Ser473}, not pAKT2^{Ser474}, parallels those of pan pAKT^{Ser473}.

PTEN subcellular localization affects its function and turnover.[10] To better understand how PTEN mutants affect their tumor suppressive functions, +AdCre+DOX-treated cultures were biochemically fractionated into plasma membrane, cytoplasmic (containing endomembranes) and nuclear extracts which were screened for PTEN by western blot. A significant reduction in nuclear PTEN levels concomitant with an increase in plasma membrane-bound fractions for PTEN G36E, L42R, C105F, C124S, G129E and R173H mutants was observed (Figure 3C). Cells expressing PTEN WT and PTEN Y138L displayed a similar pattern of subcellular compartmentalization as endogenous mouse PTEN proteins (Figure 3C). Furthermore, western blotting for EGFR and phospho-EGFR using the same subcellular fractionated extracts revealed an accumulation of $EGFR^{vIII}$ and phospho-$EGFR^{vIII}$ in endomembrane-containing cytoplasmic fractions of G36E, L42R and C124S PTEN expressing cells (Figure 3D).

Taken together, these results suggested that PTEN mutants with increased plasma membrane association are correlated with increased EGFRvIII phosphorylation on endomembranes and concomitant MAP kinase/STAT3 signaling. In addition, we noted that lipid phosphatase catalytically dead PTEN mutants (C124S, G129E and R173H) add to this through increased PIP3 and full activation of AKT. Interestingly, cells expressing G36E and L42R PTEN demonstrated that AKT activation is not necessary for cellular transformation from these mutants.

Loss of PTEN downregulates metabolic processes

To better understand the molecular outcomes of PTEN loss in the context of $EGFR^{vIII}$ signaling, we performed quantitative tandem mass tag (TMT)-based multiplexed liquid chromatography mass spectrometry (LC-MS) phosphoproteomics and analyzed[30,31] the clonally derived, isogenic $EGFR^{vIII}$;Cdkn2a$^{-/-}$;Pten$^{-/-}$ DOX-induced PTEN WT, G36E, L42 and C124S astrocytes (Figure 2A), comparing their proteomes to parental untreated cells. First, we evaluated changes in global protein expression upon loss of endogenous mouse PTEN (+AdCre) in the PTEN WT, G36E, L42R and C124S mutants isogenic clonally derived cell cultures by comparing PTEN null proteome to control cultures. A total of 9610 proteins were quantified in all samples from which those with a $Log_2FC < -1.5$ and >1.5 when compared to their untreated parental cells were subsetted (Figure S4A). We identified 949 and 356 proteins that were commonly downregulated and upregulated respectively among PTEN WT, G36E, L42R and C124S mutants (Figure S4B). Gene ontology analysis of these commonly downregulated and upregulated proteins reveal proteins that function in lipid metabolic processes, mitochondrial translation, and aerobic respiration that are downregulated upon loss of PTEN whereas proteins involved in cell cycle regulation, cell division, chromosomal segregation and mitotic cell cycle are upregulated in PTEN null cells (Figure S4C). Analyzing the proteomes of isogenic cells expressing missense mutant PTEN proteins (+AdCre +DOX) for PTEN G36E, L42R and C124S in the absence of PTEN WT revealed upregulation of proteins involved in cell cycle, cell division and chromosomal segregation and mitotic spindle organization, whereas proteins involved in immune system process, hypoxia, inflammatory response, cytokine response, and lipid metabolic process were downregulated (Figure S4D). These results demonstrate that either loss of PTEN or expression of PTEN missense mutants in the context of $EGFR^{vIII}$ overexpression and loss of Ckdn2a upregulates components of the cell cycle and mitosis, supporting the aforementioned cell division and cellular transformation results. Additional studies are necessary to decipher the details of the observed down regulations of protein associated with biological processes such as lipid metabolism, inflammatory response and response to cytokine and hypoxia upon loss of PTEN and expression of PTEN missense mutants.

Selective activation of kinases from PTEN missense mutants

Next, we measured the levels of 19,198 phosphopeptides in all samples normalized to 9610 proteins and subsetted the phosphopeptides to up- and down-regulated phosphoproteins upon complete loss of PTEN (Figure 4A). To gain mechanistic insights from these datasets, we leverage the recently established Kinase Library[32] to identify the specific kinases that are responsible for these phosphorylation events. In all of our isogenic PTEN missense mutant cell cultures, loss of PTEN resulted in significant activation of several cyclin dependent kinases (CDKs), activation of AKTs and other AGC family member kinases (Figures 4A and 4B). We also observed activation of ERK1/2, JNK1/2, NLK and P38G kinases, as well as PINK1. On the other hand, loss of PTEN resulted in the downregulation of phosphopeptides that are substrates of CDKL1, CLK1/4, and several DYRKs and HIPKs (Figures 4A and 4B). When compared to PTEN WT-expressing phosphoproteomes,

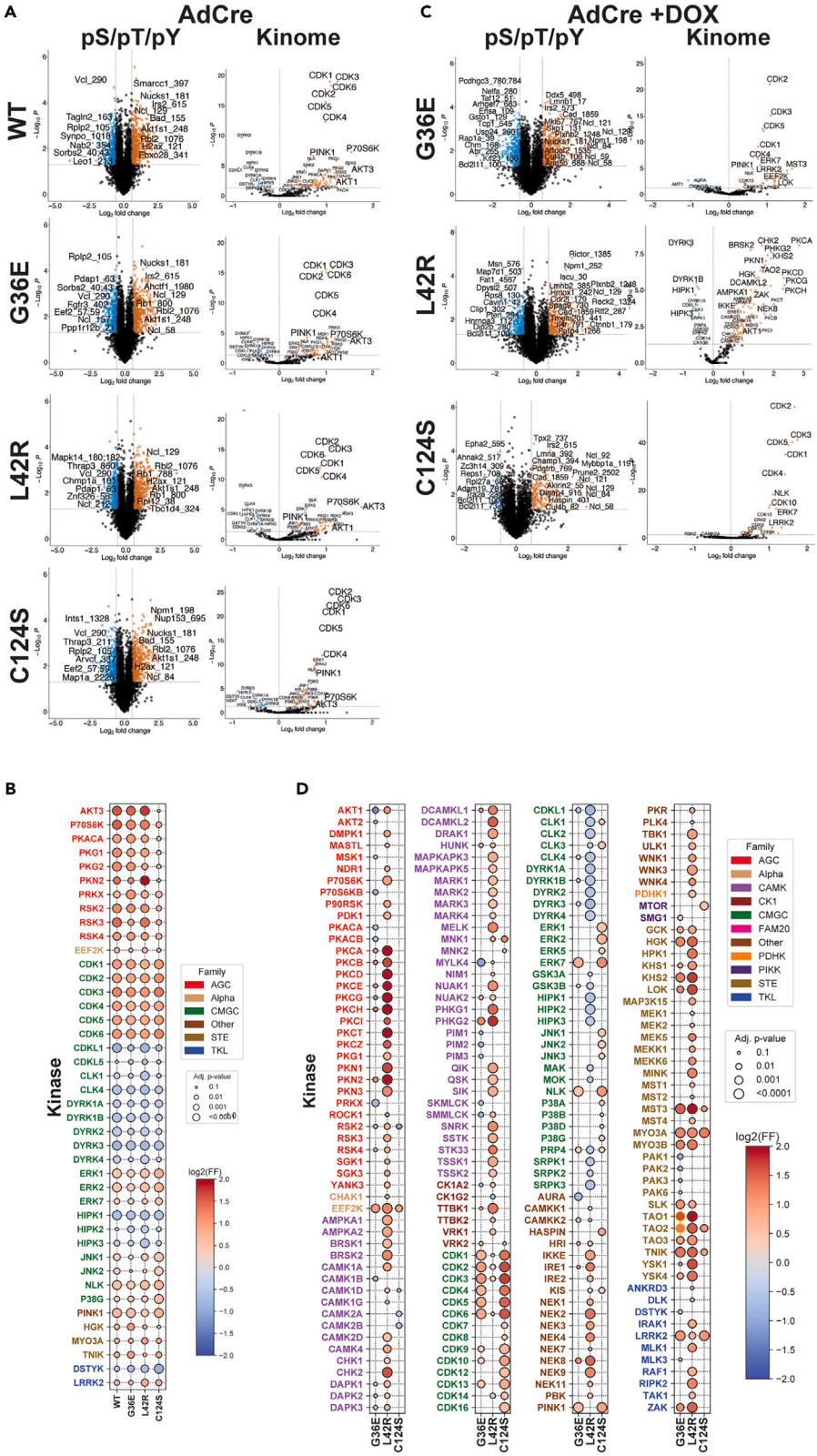
A
AdCre
pS/pT/pY
Kinome
WT
G36E
L42R
C124S
C
AdCre +DOX
pS/pT/pY
Kinome
G36E
L42R
C124S
B
Kinase
Family
AGC
Alpha
CAMK
CK1
CMGC
Other
STE
TKL
Adj. p-value
0.1
0.01
0.001
<0.0001
log2(FF)
D
Kinase
Family
AGC
Alpha
CAMK
CK1
CMGC
FAM20
Other
PDHK
PIKK
STE
TKL
Adj. p-value
0.1
0.01
0.001
<0.0001
log2(FF)

Figure 4. PTEN G36E, L42R and C124S mutants activate divergent signaling pathways

(A) Volcano plots of pS/pT/pY phosphoproteomics and Kinase Library analysis for the indicated PTEN null (+AdCre) cells. Data were obtained from biologically independent replicates, $n = 3$.

(B) Bubble plot of kinases that are activated and inhibited in all four PTEN null clonal cell cultures in (A).

(C) Volcano plots of pS/pT/pY phosphoproteomics and Kinase Library analysis for the indicated PTEN mutant (+AdCre +DOX) expressing cells.

(D) Bubble plot of kinases that are significantly activated and inhibited in the indicated PTEN null clonal cell cultures in (C).

PTEN G36E, L42R and C124S expressing cells exhibited much more variations in their kinome usage. For example, in PTEN L42R-expressing cells, we observed robust upregulations of phosphosites matching the motifs of AMPKA, BRSK, and MARK, suggesting that these cells are experiencing energy stress, as well as predicted upregulation of the PKC, MAPKAPK, and various MAP3K family members and down regulation of a group of less-well studied kinases that include CLK, DYRK, HIPK and SRPK family members (Figures 4C and 4D). On the other hand, PTEN G36E expressing cells, when compared to PTEN WT expressing cells showed activation of CDK family members, Erk7, and NLK and downregulation of PKACs, PRKX, MYLK4, PIMs, and AURA kinase activity (Figures 4C and 4D). Lastly, expression of the phosphatase null PTEN C124S led to the activation of CDKs, ERKs, JNKs, PINK1, and MTOR kinase activity.

Restoration of PTEN expression slows tumor growth and prolongs survival

Restoration of tumor suppressor gene expression post tumor formation result in rapid and drastic elimination of tumors.[33] To determine if cancers driven by PTEN deficiency are similarly addicted to PTEN loss in mice, we induced expression of PTEN WT in EGFR^{vIII};*Ckdn2a*$^{-/-}$;*Pten*$^{-/-}$ clonal astrocyte cultures implanted subcutaneously in immunodeficient mice at two time points during the growth of tumors (Figure 5A). Re-expression of PTEN WT after 24- and 36-day post-injection led to significant reduction in tumor growth (Figure 5A) and tumor volume (Figure 5B) with the most potent effect observed when PTEN is reactivated after 24 days post injection.

To determine the effects of re-expressing PTEN WT post tumor initiation on overall survival, we leveraged our compound, genetically engineered mouse (GEM) model of GBM,[6] which consists of a conditional overexpression of the human EGFR^{vIII} cDNA under the control of a transcriptional/translational stop (Lox-STOP-Lox, LSL) cassette present on a Cdkn2a$^{tm1Rdp/tm1Rdp}$ constitutive knock out strain[34] and a conditional Pten$^{tm1Hwu/tm1Hwu}$ (PTEN^{2lox}) strain.[35] Using this model, we previously observed that CNS expression of EGFR^{vIII} in the context of *Cdkn2a* loss is insufficient to generate GBM lesions in mice, requiring additional loss of *Pten* to initiate GBM *in vivo*.[6] To facilitate noninvasive monitoring of tumor growth, we crossed our (LSL)EGFR^{vIII};Cdkn2a$^{-/-}$;PTEN$^{2lox/2lox}$ strain to our conditional LSL-Luciferase (Luc)[36] mice to create a compound LSL-EGFR^{vIII};Cdkn2a$^{-/-}$;PTEN$^{2lox/2lox}$;LSL-Luc. Exposure to Cre recombinase removes the LSL cassettes resulting in expression of EGFR^{vIII} and firefly luciferase and deletion of the endogenous mouse Pten$^{2lox/2lox}$ gene. To deliver Cre, we created a multi-functional lentivirus that express iCre recombinase and a DOX-inducible human PTEN WT cDNA (Figure S5A). We generated cohorts of LSL-EGFR^{vIII};Cdkn2a$^{-/-}$;PTEN$^{2lox/2lox}$;LSL-Luc mice stereotactically injected with this lentivirus. In the absence of DOX, these animals develop fully penetrant GBMs with a median survival of 51.5 days post lentiviral injection (Figure 5C). On the other hand, administration of DOX concurrent to stereotactic intracranial injection of the lentivirus led to ectopic expression of human PTEN WT and prevented GBM formation (Figure 5C). Withdrawal of DOX in the latter cohort of animals at 86 days post-lentiviral injection resulted in GBM formation as monitored using bioluminescence imaging (Figure 5D). Human PTEN WT expression was attenuated (Figures 5E and S5B), with full penetrance and an abbreviated median survival of 16 days from the time of DOX withdrawal (Figure 5C). The detectable levels of PTEN in these tumors are due to the presence of various PTEN positive cell types among PTEN negative neoplastic cells. Finally, we previously determined that a $>10^7$ p/s/cm^2/sr BLI output in this model indicates the presence of early GBM lesions.[6,37,38] Using this metric to determine presence of GBM tumors, we administered DOX to tumor-bearing animals that had reached $>10^8$ p/s/cm^2/sr BLI output to re-express PTEN WT at levels comparable to endogenous mouse PTEN (Figures 5E and S5C) and showed a significant prolongation in median survival (-DOX 6.5 days vs. +DOX 18.0 days post tumor detection) (Figures 5F and 5G). In these experiments, retention of EGFR^{vIII} expression was confirmed by immunohistochemistry (Figure S5D). These results demonstrate an absolute requirement for loss of PTEN function for EGFR^{vIII}-driven gliomagenesis and show that PTEN re-expression post tumor formation significantly prolongs survival.

PTEN missense mutants have dominant-negative attributes and form GBM in mice

PTEN's ability to homodimerize forms the basis of phosphatase-null mutants' ability to behave in a dominant-negative manner.[18] We ascertained the capacity of our allelic series of missense PTEN mutants to function in a dominant-negative fashion *in vitro* and *in vivo*. Treating our EGFR^{vIII};Cdkn2a$^{-/-}$;PTEN$^{2lox/2lox}$ clonally derived PTEN mutants astrocyte cultures with +DOX in soft agar growth assays demonstrated cellular transformation for all mutants except PTEN WT and Y138L (Figures 6A and 6B). Subcutaneous injection of these astrocytes expressing PTEN mutants in immunocompromised mice administered DOX revealed that, *in vivo*, expression of PTEN G36E, L42R, C105F, and C124S in the presence of endogenous WT mouse PTEN resulted in cancer cell growth, indicating dominant negative activity in this context. PTEN L42R expressing cells grew the fastest and G36E the slowest (Figures 6C and 6D). In contrast, expression of PTEN G129E and R173H was insufficient to overcome WT activity and generate tumor growth *in vivo* even though they were adequate to transform EGFR^{vIII};Cdkn2a$^{-/-}$ astrocytes *in vitro*, suggesting an inability to surpass higher environmental thresholds for transformation *in vivo*.

Next, we assessed the capacity of PTEN G36E, L42R and C124S to initiate gliomagenesis in a dominant-negative manner in an autochthonous genetically engineered model. To recreate a genomically realistic condition, we utilized a hemizygous PTEN$^{2lox/+}$ genotype to generate cohorts of LSL-EGFR^{vIII};Cdkn2a$^{-/-}$;PTEN$^{2lox/+}$;LSL-Luc mice (Figure S6A) that were stereotactically injected with iCre lentiviruses expressing

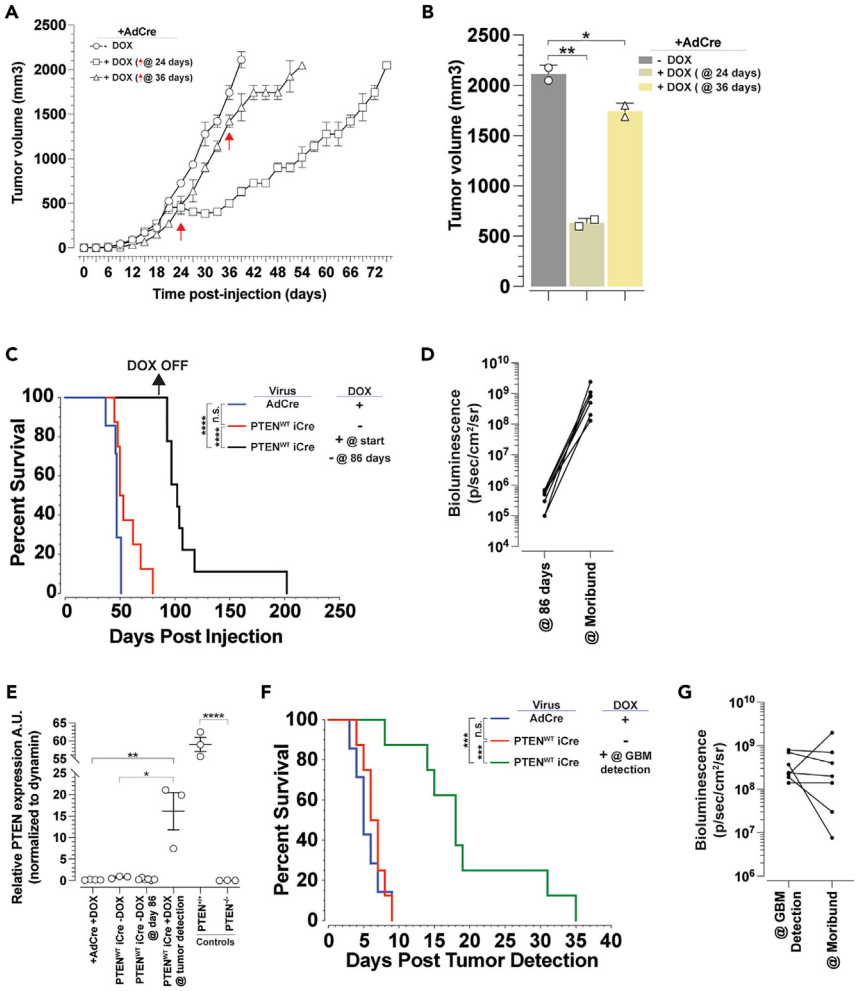

Figure 5. Reactivation of PTEN expression post GBM formation prolongs survival

(A and B) Tumor growth kinetics of subcutaneous EGFR^{vIII};Cdkn2a$^{-/-}$;PTEN$^{-/-}$ astrocytes (n = 2) in immunocompromised mice with activation of PTEN WT expression at the indicated time points (A) and quantitation of tumor volumes at 39 days post inoculation (B). Data are presented as the mean +/- S.D. of biological replicates, unpaired t test, two-tailed, *p<0.05 and **p<0.001.

(C) Wild type PTEN expression prevents GBM formation. Kaplan-Meier survival of EGFR^{vIII};Cdkn2a$^{-/-}$;PTEN$^{2lox/2lox}$ genetically engineered mice injected with conditional lentivirus expressing human PTEN WT and constitutive iCre recombinase. Treatments of intracranial *de novo* GBM mice with (+DOX) and without (-DOX) expression of PTEN are indicated. All control mice succumbed to GBM at 86 days post tumor initiation, at which point DOX was withdrawn in the experimental cohort.

(D) Quantitation of bioluminescence imaging data of (C).

(E) Quantitative western blotting of tumor lysates from (C) for PTEN expression for the indicated conditions. Controls are PTEN$^{+/+}$ and PTEN$^{-/-}$ mouse GBM cell lines. Data are presented as the mean ± S.E.M. of biologically independent replicates, n=>3, unpaired t test, two-tailed, *$p < 0.05$, **$p < 0.01$, ***$p < 0.001$ and ****$p < 0.0001$.

(F) Reactivation of wild type PTEN once GBM have formed prolong survival. Intracranial GBM tumors were initiated in cohort of EGFR^{vIII};Cdkn2a$^{-/-}$;PTEN$^{2lox/2lox}$ genetically engineered mice using DOX inducible PTEN WT expression lentivirus with constitutive iCre expression and tumorigenesis monitored by BLI. Once GBM are detected (BLI output >10^7 p/s/cm^2/ser), controls remained untreated and experimental cohort was subjected to reactivation of PTEN (+DOX).

(G) Quantitation of bioluminescence imaging data of (F).

DOX-inducible PTEN mutants (Figure S6A). Administration of +DOX in these mice and longitudinal monitoring using BLI revealed the formation of fully penetrant intracranial tumors (Figures 6E and 6F) with median survivals between 39 and 45 days post tumor detection (@BLI >10^7 p/s/cm^2/sr) (Figure 6G). In the absence of DOX, animals did not develop intracranial neoplasms due to the tumor suppressive function of the one remaining copy of the endogenous mouse WT PTEN allele (Figures S6B and S6C). Histopathologically, end-stage tumors are extensive and composed of moderate to densely cellular glial neoplasms (Figure 6H). Further analysis revealed the presence of pseudopalisading necrosis (Figures 6I–6i), vascular proliferation (Figures 6I–6ii), perivascular infiltration (Figures 6I–6iii), focal infiltration of brain tissue (Figures 6I–6iv), frequent mitoses (Figures 6I–6V), and leptomeningeal spread (Figures 6I–6vi). Overall, these histological features are

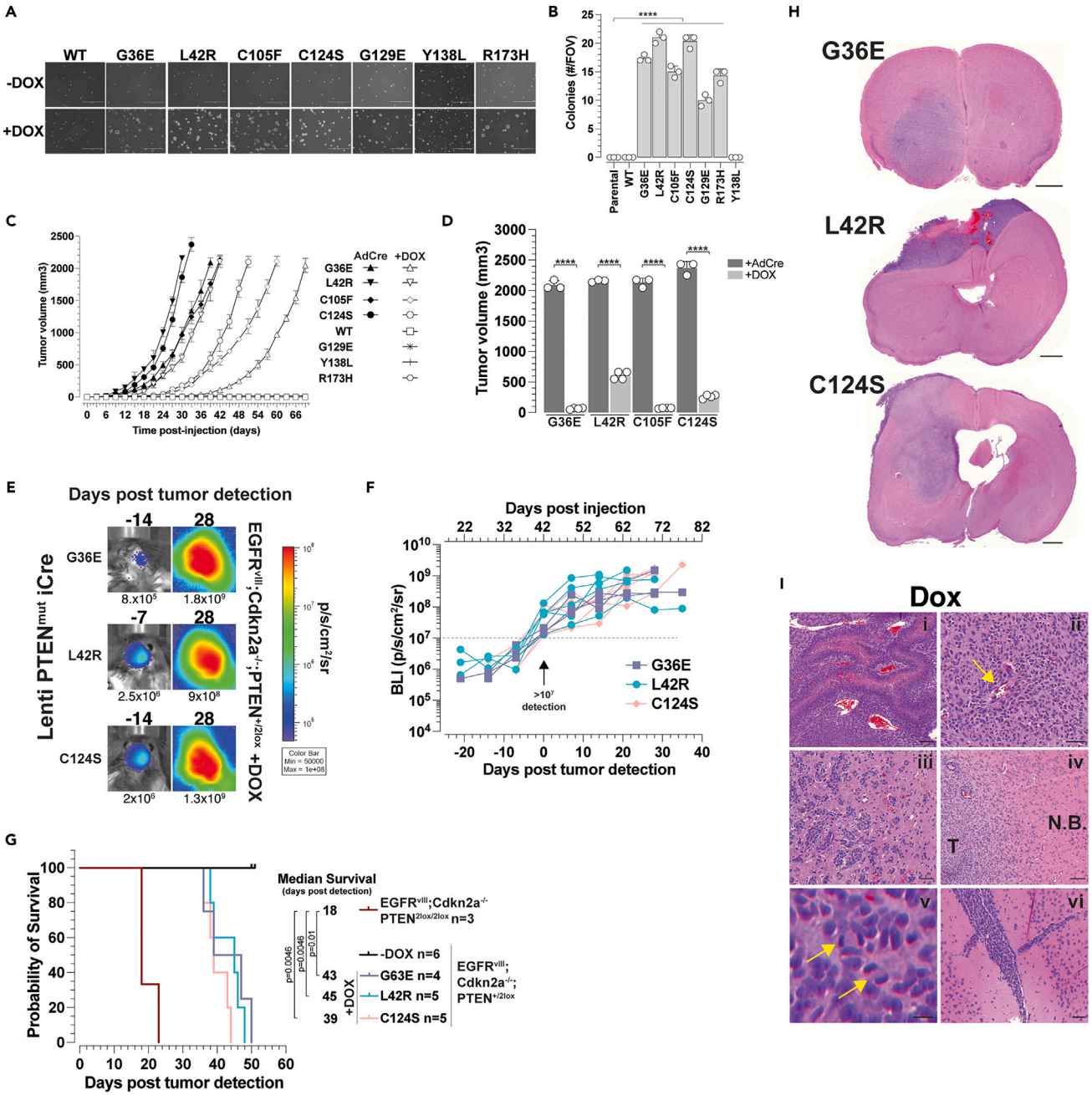

Figure 6. Dominant-negative attributes of PTEN mutants *in vivo*

(A and B) Representative photomicrographs (A) and quantitation (B) of *in vitro* growth in soft agar assays for the indicated PTEN mutants expressed in the presence of endogenous mouse PTEN protein. Scale bar = 400 μm. Data are presented as the mean +/- S.E.M of biological replicates n=3, unpaired t test, two-tailed, ****p<0.0001.

(C and D) Tumor growth kinetics of subcutaneous EGFR^{vIII};Cdkn2a$^{-/-}$;PTEN$^{+/+}$ astrocytes with inducible (+DOX) expression of the indicated PTEN mutants (n=>3) in immunocompromised mice (C) and quantitation of tumor volumes at maximally tolerated tumor size (>2000 mm^3) for PTEN null and mutant PTEN expression in PTEN$^{+/+}$ conditions (D). No tumors were detected in PTEN WT, G129E, Y138L and R173H + DOX treatments. Tumor growth curves for PTEN WT, G129E, Y138L and R173H + AdCre treatments were omitted for clarity and can be viewed in Figure S2I. Data are presented as the mean +/- S.E.M of biological replicates, unpaired t test, two-tailed, ****p<0.0001.

(E and F) Representative bioluminescence images (E) and quantitation (F) of mice expressing the indicated PTEN mutants in EGFR^{vIII};Cdkn2a$^{-/-}$;PTEN$^{+/2lox}$ genetically engineered mice. Mice were administered a DOX diet on day 0 of injection.

(G) Kaplan-Meier survival analysis of the indicated PTEN mutant expressed in the context of endogenous mPTEN.

Figure 6. *Continued*

(H) Representative H&E stained FFPE sections of GBMs expressing the indicated mutant PTEN in the presence of endogenous mPTEN. Scale bars = 1 mm.
(I) Representative photomicrographs of histopathological analysis of H&E stained FFPE sections of GBMs in (H) showing i-pseudopalisading necrosis, ii-endothelial proliferation (arrow), iii-perivascular infiltration, iv-diffuse invasion of tumor cells (T) into normal brain (N.B.), v-mitotic figures (arrows), and vi-meningeal infiltration. Scale bars i,iv = 100 μm, ii,iii,vi = 50 μm and v = 10 μm.

consistent with GBM. Through these results, we demonstrate that PTEN G36E, L42R and C124S are capable of dominant negative neoplastic function(s) *in vitro* and *in vivo*.

Dominant-negative PTEN missense mutants activate distinct signaling networks

To gain insights into the PTEN missense mutations ability to induce cellular transformation, we performed western blot analyses for PTEN canonical signaling proteins using our isogenic cells treated with +DOX (Figures 3B and S3). Missense PTEN mutant proteins were expressed in the presence of endogenous mouse PTEN. Unlike loss of PTEN or sole expression of PTEN missense mutants (in the absence of endogenous mouse PTEN), co-expression of WT and mutant PTEN did not result in activation of EGFR kinase activity nor in any of the pathway members previously identified (Figures 3B and S3B), suggesting that their dominant-negative mode of action during the transformation process are different than the canonical pathways controlled by PTEN.

To better understand how the expression of PTEN mutants function in a dominant-negative context, we evaluated the changes in global protein expression upon expression of the PTEN missense mutants in the presence of endogenous mouse PTEN. We performed quantitative TMT-based multiplexed LC-MS proteomics and analyzed[30,31] clonally derived, isogenic EGFR^{vIII};Cdkn2a$^{-/-}$;Pten$^{2lox/2lox}$ DOX-induced PTEN WT, G36E, L42R, C105F, C124S, G129E, Y138L and R173H astrocytes, comparing their proteomes to untreated cells. A total of 7619 proteins were quantified in all samples from which those with a $Log_2FC < -1.25$ and >1.25 when compared to their untreated parental cells were subsetted (Figures 7A and S7A). We found that expression of transforming (*in vitro*) PTEN mutants G36E, L42R, C105F, C124S, G129E and R173H led to upregulation of proteins involved in ribosome biology and protein translation, mitochondrial function, and metabolism (Figures 7A and S7A). These gene ontologies were not upregulated in the PTEN mutants WT and Y138F that failed to transform astrocytes (Figure 7A). Conversely, expression of dominant-negative PTEN mutants G36E, L42R, C105F, C124S, G129E and R173H resulted in downregulation of proteins that are linked to aerobic respiration, oxidative phosphorylation, and response to stress. Similarly, these ontologies were not downregulated in the PTEN mutants (WT and Y138F) that failed to transform astrocytes (Figure 7A). Next, we measured the levels of 4209 phosphopeptides in all samples normalized to 7619 proteins and subsetted the phosphopeptides to up- and down-regulated phosphoproteins upon DOX-induced expression of PTEN mutants. Normalized phosphoproteome analysis (Figure 7B) did not reveal common phosphorylated proteins amongst all PTEN mutants (G36E, L42R, C105F, C124S, G129E and R173H) acting in a dominant-negative manner to transform astrocytes. Instead, we observed specific up- and down-regulated phosphorylation events in transforming and non-transforming PTEN mutants (Figure 7B). Together, these results indicate that expression of PTEN missense mutants G36E, L42R, C105F, C124S, G129E and R173H in the presence of endogenous mouse PTEN WT proteins activate signaling events that are related to mutation classes.

PTEN missense mutants homodimerize

PTEN has been shown to function as a homodimer and as such, mutant PTEN proteins can act in a dominant negative fashion by inactivating the function of WT PTEN.[18] To determine if PTEN G36E, L42R and C124S missense proteins can interact with PTEN WT in cells, we created N- and C-terminal HaloTag[39] fusion human PTEN hybrid proteins expression systems using an inducible, doxycycline (DOX)-regulated lentivirus. HaloTag PTEN mutants G36E, L42R, C124S, and PTEN WT and a HaloTag control were expressed in EGFR^{vIII};Cdkn2a$^{-/-}$;PTEN^{2lox} astrocytes in a DOX-dependent manner (Figures S8A and S8B). To validate proper subcellular localization of the HaloTag PTEN fusion proteins, cells were treated with AdCre to delete endogenous mouse PTEN protein, with and without DOX treatment to induce PTEN. Subcellular fractions were isolated and HaloTag PTEN fusions detected by western blots using anti-PTEN and anti-HaloTag antibodies (Figures 8A and 8B, S8C and S8D). These results demonstrate that fusing PTEN proteins to HaloTag does not impact their subcellular distribution. To determine if mutant PTEN proteins interact with endogenous mouse PTEN, the expression of HaloTag-PTEN fusion proteins was induced in EGFR^{vIII};Cdkn2a$^{-/-}$;PTEN^{2lox} astrocytes with DOX for 24 h and HaloTag-PTEN proteins affinity purified. Bound proteins were stripped and subjected to quantitative tandem mass tag (TMT)-based multiplexed LC-MS. When compared to control Halo-bound proteins, Halo-PTEN WT, G36E, L42R and C124S fusion protein consistently co-affinity purified endogenous mouse PTEN (Figure 8C). Together, these results suggest that HaloTag PTEN fusion proteins interact with endogenous mouse PTEN protein, an observation in agreement with PTEN's homodimerization capacity.

DISCUSSION

PTEN's tumor suppressive functions are complex and context dependent, and mechanistic details pertaining to specific mutations are lacking. Using an EGFR^{vIII}-driven isogenic system that is entirely dependent on PTEN function for cellular transformation *in vitro* and GBM formation *in vivo*, we dissected the activities of several clinically relevant PTEN missense mutations. In our system, complete loss of PTEN expectedly elevated PIP3 levels and stimulated AKT activity. Surprisingly however, loss of PTEN was also associated with elevated phospho-EGFR^{vIII} levels and activated an MEK/ERK/STAT3 signaling axis. Cells with PTEN loss underwent cellular transformation *in vitro* and formed tumors in mice

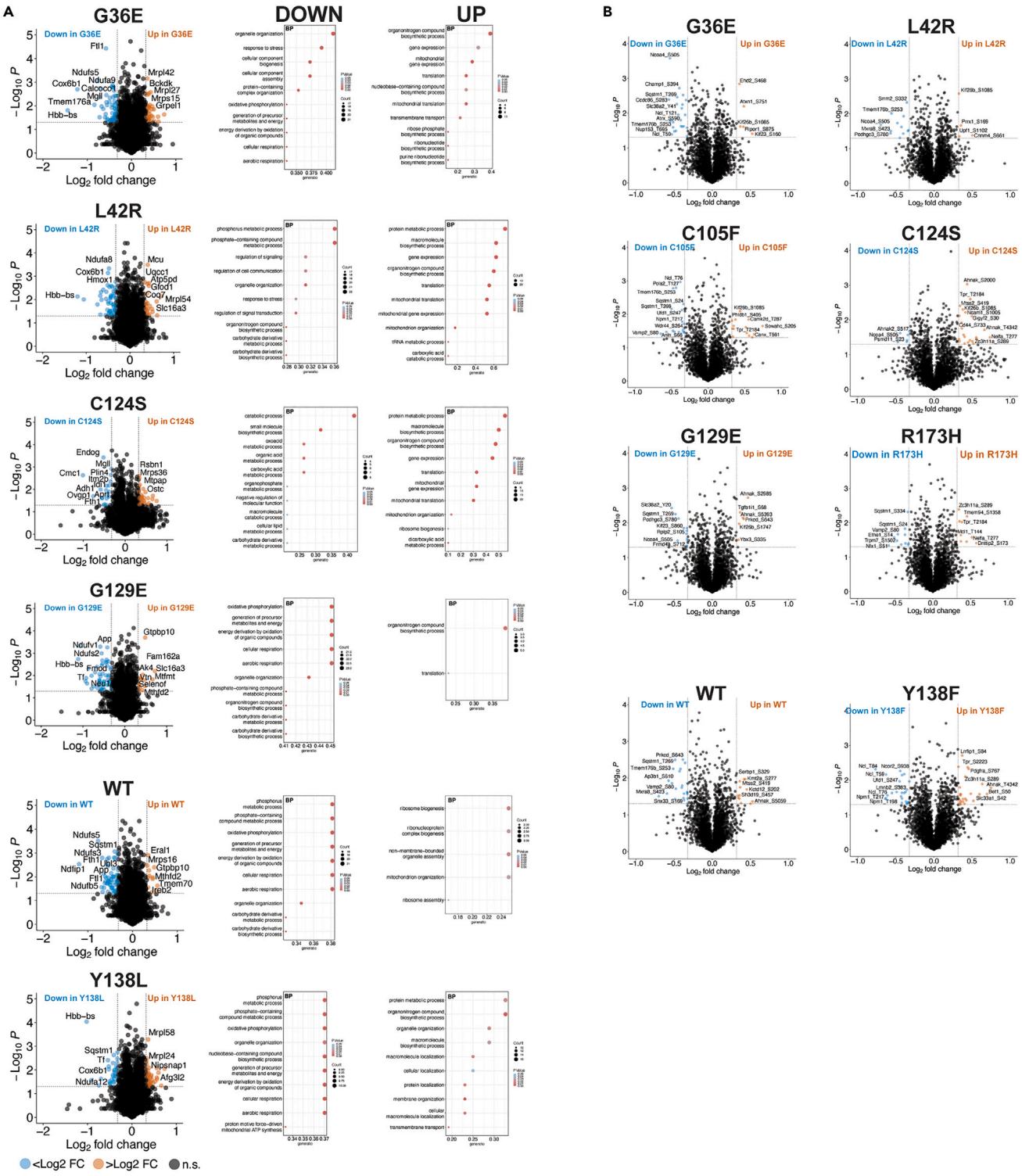

Figure 7. Activation of distinct proteome and signaling networks from dominant-negative PTEN missense mutants

(A) Volcano plots of up and down regulated proteins upon expression of missense mutants in the presence of endogenous WT PTEN (+DOX) in the indicated clonal cell cultures and GO analysis of the downregulated and upregulated proteins from the indicated clonal cell cultures. BP, Biological Processes. Data were obtained from biologically independent replicates, $n = 3$.

(B) Volcano plots of pS/pT/pY phosphoproteomics analysis from clonal cell cultures of the indicated PTEN mutants (+DOX) expressed along with endogenous mouse PTEN. Data were obtained from biologically independent replicates, $n = 3$.

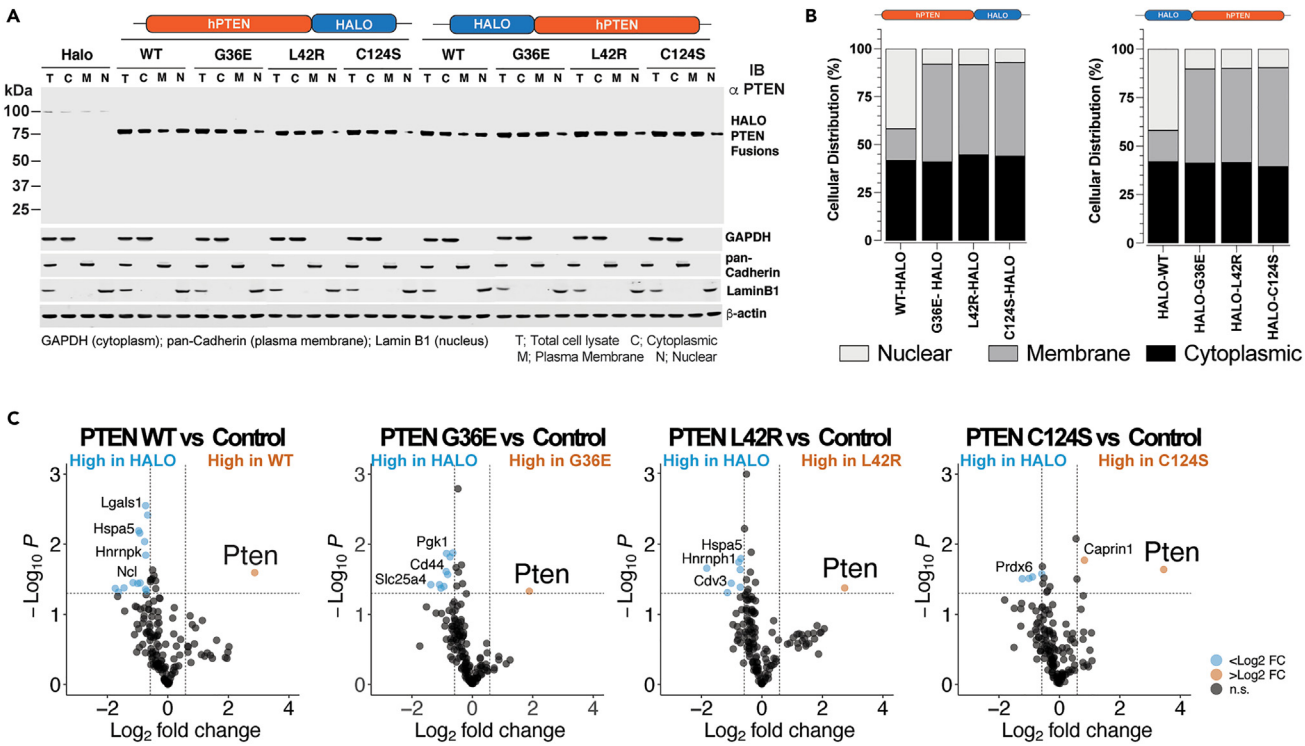

Figure 8. Missense PTEN mutants homodimerizes with PTEN WT

(A) Western blotting for expression and subcellular localization of HALO-PTEN fusion proteins in EGFR^{vIII};Cdkn2a$^{-/-}$;PTEN^{2lox} astrocytes.

(B) Quantification of (A).

(C) Volcano plots of HALO control and HALO-PTEN purified proteins from EGFR^{vIII};Cdkn2a$^{-/-}$;PTEN^{2lox} astrocytes. Data were obtained from biologically independent replicates, $n = 3$.

(summarized in Table ST2). PTEN deletion led to global changes in protein expression that supported elevated cell division and phospho-proteomics and kinase library analysis mechanistically supported a pro-mitotic phenotype.

Re-expression of human PTEN WT and mutant proteins yielded informative results. Expression of either PTEN WT or the protein phosphatase null mutant Y138L completely reversed the transformation of these cells, along with a reduction in phospho-EGFR^{vIII}, MEK/ERK/STAT3 signaling axis, decreasing the levels of PIP3 and abrogating AKT activation back to basal levels. These results demonstrate that human PTEN functions in mouse astrocytes and that the protein phosphatase activity of PTEN is not required for its tumor suppressive functions. On the other hand, re-expression of the lipid phosphatase null PTEN C124S, G129E and R173H[23] resulted in elevated phospho-EGFR^{vIII} levels and activated MEK/ERK/STAT3 signaling axis, retaining high levels of PIP3 and AKT activation. Expression of PTEN C105F, a mutant with reduced phosphatase activity,[23] also resulted in high phospho-EGFR^{vIII} levels and activated MEK/ERK/STAT3 signaling and did not reduce PIP3 levels beyond the threshold level necessary for AKT activation. We thus show that the lipid phosphatase activity of PTEN is not required to activate phospho-EGFR^{vIII}. Re-expression of PTEN G36E and L42R reduced PIP3 and AKT activation down to basal levels, demonstrating that these two mutants retain lipid phosphatase activity in cells. Our results with PTEN G36E and R173H are different from observations made in a reconstituted yeast system, where expression on G36R displayed low PTEN PTPase activity and expression of R173H displayed intermediate PTPase activity,[40] contrasting ours where PTEN G36E displayed full PTPase activity and PTEN R173H none. This discrepancy is perhaps due to the divergent model systems used to assess similar attributes and/or the type of change at G36, discerning the acquisition of a negative charge (G36E) compared to a positive charge (G36R). Similarly, in yeast and drosophila systems, PTEN G36E was reported to have no functional activity, whereas PTEN R173H displayed activity but not R173P.[41] Although PTEN L42R retention of catalytic activity has been demonstrated *in vitro*,[23] our studies on PTEN G36E expression *in vivo* shed light on this mutation. Expression of PTEN G36E and L42R also resulted in high phospho-EGFR^{vIII} levels and activated MEK/ERK/STAT3 signaling, demonstrating that PTEN's influence on phospho-EGFR and phospho-MEK/ERK/STAT3 levels are independent from AKT activation.

All PTEN mutants studied except R173H and C105F displayed stable protein levels. Our results are comparable to previous studies of PTEN protein stability in yeast and mammalian cells that showed a ~2/3 decrease in stability for PTEN R173H when compared to WT.[41] In addition to destabilizing PTEN, mutations at R173H and C105F also affect the lipid phosphatase catalytic activity of PTEN, thus compromising PTEN enzymatic and non-enzymatic functions. It is unclear why PTEN R173 missense mutants are highly prevalent in GBM, but this potentially reflects the need to inactivate both enzymatic and non-enzymatic functions of PTEN during gliomagenesis. How R173 and C105 mutations molecularly destabilize PTEN remains to be determined.

PTEN acts on membranes and in the nucleus where it controls various cellular phenotypes.[42] Two modes of PTEN-association with membranes have been described (reviewed in[43]): transient plasma membrane binding mediated by electrostatic charge interactions and steady state endosomal membrane binding mediated by the PTEN C2 domain as a reader of the PI(3)P endosomal lipid.[44] In the cytoplasm, PTEN is found as a self-inhibited monomer due to interactions between phosphorylation of a Ser/Thr cluster within the C-terminal tail and membrane binding interface of the phosphatase and C2 domains. Dephosphorylation of the C-terminal tail releases the autoinhibition and facilitate translocation of PTEN to membranes (reviewed in[43]). Using subcellular fractionation techniques, we observed that, with the exception of PTEN WT and Y138L, all mutants studied displayed significant increases in membrane binding concomitant with decreases in nuclear localization and no change in cytoplasmic fraction. Given that PTEN nuclear import is an active process, requiring monoubiquitination on K289 and K13,[10] it is possible that the increased plasma membrane association observed precludes nuclear import of PTEN. Our observation of PTEN R173H membrane localization is in contrast to a previous study using immunofluorescence of PTEN R173C in a reconstituted U87 cell system that reported PTEN R173C localization to the nucleus.[45] Perhaps this discrepancy is the result of using of vastly different model system and techniques to detect localization. Nevertheless, this increased plasma membrane association is independent of phosphatase catalytic activity since both lipid PTPase active (G36E, L42R and to a certain degree C105F) and inactive (C124S, G129E, R173H) demonstrated increased localization to the plasma membrane. The mechanism by which such a diverse group of PTEN mutants preferentially accumulates at the plasma membrane will be a topic of further study. Our results showing PTEN L42R increased targeting to plasma membranes is opposite of reported decreases in plasma membrane association for this mutant when studied in *Dictyostelium discoideum*,[46–48] perhaps reflecting differences in model system and techniques (C-terminal GFP fusion protein) used to study localization. The PI (4,5)P2-binding domain (PBD) is responsible for PTEN's binding to PIP2 anionic lipids, which is accomplished by the formation of a distinct lipid-binding pocket, created with the carboxyl terminus of the PBD and nearby portions of the phosphatase domain.[49] G36E and L42R reside within this pocket and therefore it is possible that these mutations enhance PIP2 binding and affinity to plasma membrane.

Complete loss of PTEN or dysregulation of PTEN localization to the plasma membrane correlated with elevated levels of phospho-EGFR^{vIII} and MEK/ERK/STAT3 pathway activation and the transformation of astrocytes. The exact mechanisms by which these events are related remains to be established, however, signals emanating from activated and phosphorylated EGFR receptors are largely attenuated by receptor endocytosis and endosomal sorting where EGFR is either recycled or degraded and dephosphorylated.[50] Given the accumulation of EGFR^{vIII} and phospho-EGFR^{vIII} on endomembranes in PTEN mutant expressing cells (Figure 3D), it is therefore possible that elevated plasma membrane PTEN levels plays a role in regulating endocytosis and recycling of cell surface proteins including EGFR^{vIII} and thus regulates EGFR^{vIII} phosphorylation through a yet unidentified function for plasma membrane PTEN in endocytosis. We also demonstrated that, in two different mouse models, re-expression of PTEN WT function post tumor formation is efficient at slowing down tumor growth and significantly extended survival, underscoring the potential clinical application of this approach.

A significant finding from our studies is the ability of G36E and L42R PTEN mutants to drive tumorigenesis in a PIP3-AKT independent manner. There have been several reports of lipid phosphatase independent tumor suppressor functions of PTEN (reviewed in[10,11,51]), most of which describing mechanisms of mis-localized or altered scaffolding functions of PTEN. Having shown that these two mutants displayed elevated plasma membrane association, we investigated the effects that these mutants have on global signaling network using quantitative phosphoproteomics and kinome analysis. This revealed that both mutants modulate overlapping and specific signaling events, highlighting the pleiotropic nature of PTEN function. Finally, PTEN was recently shown to dimerize, making catalytically inactive mutants capable to function in a dominant-negative manner.[18,52] Here we revealed dominant-negative functions for PTEN G36E, L42R, C105F, C124S, G129E, and R173H *in vitro* and in a genetically engineered mouse model. Surprisingly, proteomic and phosphoproteomic analyses revealed divergent usage of global signaling for all PTEN mutants. Expression of PTEN G36E, L42R, C105F, C124S, G129E, and R173H in the presence of PTEN WT led to increase in expression of protein ontologies that are highly supportive of rapidly dividing cells.

In conclusion, using clinically relevant GBM-centric PTEN missense mutants in an isogenic inducible system, we revealed important modes of tumor suppressive function for PTEN. We discovered that PTEN regulates EGFRvIII phosphorylation and signaling in a lipid phosphatase independent manner and that the global signaling networks of PTEN mutants support cell division, albeit in independent manners.

Limitations of the study

Although our results are compelling, there are a few limitations to our studies. For example, we cannot study the functions of the PTEN mutants in the absence of endogenous mouse PTEN in the genetically engineered model because loss of mouse PTEN in itself will promote GBM formation and growth. Our model, as currently designed, can only be used to study dominant negative functions of missense mutations.

RESOURCE AVAILABILITY

Lead contact

Further information and requests for resources and reagents should be directed to and will be fulfilled by the lead contact, A.C. (acharest@bidmc.harvard.edu).

Materials availability

Presented materials are made available upon reasonable request to the lead contact.

Data and code availability

Data: Proteomics data are available at proteomexchange.org under project name "Pleiotropic tumor suppressive functions of PTEN missense mutations during gliomagenesis", accession number: PXD051485.

Code: No code was generated in this study. Any additional information required to reanalyze the data reported in this paper is available from the lead contact upon request.

ACKNOWLEDGMENTS

This work was supported by NIH grants R01 CA229784 and R21 CA245337 to AC and R01 CA275128, 5P30 CA45508 to LCT. The mass spectrometry proteomics data have been deposited to the ProteomeXchange Consortium via the PRIDE[53] partner repository with the dataset identifier PXD051485. Reviewers token information: Username: reviewer_pxd051485@ebi.ac.uk, Password: tM0xLDAH.

AUTHOR CONTRIBUTIONS

Conceptualization, S.P.G., L.C.T., and A.C.; Methodology, H.J..J., V.A.A., and A.C.; Formal Analysis, T.M.Y.-B., J.L.J., H.V., and A.C.; Investigation, H.J.J., V.A.A., J.A.P., A.T.Y., and V.A.R.; Writing – Original Draft, A.C.; Writing – Review and Editing, S.K., L.C.T., and A.C.; Funding Acquisition, L.C.T. and A.C.; Supervision, S.P.G., L.C.T., and A.C.

DECLARATION OF INTERESTS

The authors declare no competing interests.

STAR★METHODS

Detailed methods are provided in the online version of this paper and include the following:

- KEY RESOURCES TABLE
- EXPERIMENTAL MODEL AND STUDY PARTICIPANT DETAILS
  - $EGFR^{VIII}$ conditional mice and primary astrocyte cell cultures
  - Intracranial stereotactic injections
  - Bioluminescence
  - Tumor growth in immunocompromised mice
- METHOD DETAILS
  - Histology and immunohistochemistry
  - Soft agar assay
  - Immunoblot
  - PTEN mutants, HaloTag fusion and virus construct design, production and titer determination
  - Immunofluorescence
  - EGFR trafficking
  - Flow cytometry
  - Cellular fractionation
  - Quantitative reverse transcriptase polymerase chain reaction
  - Cellular PIP3 analysis
  - HaloTag PTEN fusion proteins
  - Proteomics and phosphoproteomics
  - Liquid chromatography and tandem mass spectrometry (whole proteome)
  - Liquid chromatography and mass spectrometry data acquisition (whole proteome)
  - Liquid chromatography and tandem mass spectrometry (phosphoproteome)
  - Data analysis
  - Quantification and normalization of TMT data
  - Proteomic differential abundance analysis
  - The kinase library analysis
- QUANTIFICATION AND STATISTICAL ANALYSIS

SUPPLEMENTAL INFORMATION

Supplemental information can be found online at https://doi.org/10.1016/j.isci.2024.111278.

Received: April 8, 2024
Revised: October 24, 2024
Accepted: October 25, 2024
Published: October 28, 2024

REFERENCES

1. Brennan, C.W., Verhaak, R.G.W., McKenna, A., Campos, B., Noushmehr, H., Salama, S.R., Zheng, S., Chakravarty, D., Sanborn, J.Z., Berman, S.H., et al. (2013). The somatic genomic landscape of glioblastoma. Cell *155*, 462–477. https://doi.org/10.1016/j.cell.2013.09.034.

2. Cancer Genome Atlas Research Network, Brat, D.J., Verhaak, R.G.W., Aldape, K.D., Yung, W.K.A., Salama, S.R., Cooper, L.A.D., Rheinbay, E., Miller, C.R., Vitucci, M., et al. (2015). Comprehensive, Integrative Genomic Analysis of Diffuse Lower-Grade Gliomas. N. Engl. J. Med. *372*, 2481–2498. https://doi.org/10.1056/NEJMoa1402121.

3. McLendon, R., Friedman, A., Bigner, D., Van Meir, E.G., Brat, D.J., Mastrogianakis, M., Olson, J.J., Mikkelsen, T., Lehman, N., Aldape, K., et al. (2008). Comprehensive genomic characterization defines human

glioblastoma genes and core pathways. Nature *455*, 1061–1068. https://doi.org/10.1038/nature07385.

4. Verhaak, R.G.W., Hoadley, K.A., Purdom, E., Wang, V., Qi, Y., Wilkerson, M.D., Miller, C.R., Ding, L., Golub, T., Mesirov, J.P., et al. (2010). Integrated genomic analysis identifies clinically relevant subtypes of glioblastoma characterized by abnormalities in PDGFRA, IDH1, EGFR, and NF1. Cancer Cell *17*, 98–110.
5. An, Z., Aksoy, O., Zheng, T., Fan, Q.W., and Weiss, W.A. (2018). Epidermal growth factor receptor and EGFRvIII in glioblastoma: signaling pathways and targeted therapies. Oncogene *37*, 1561–1575. https://doi.org/10.1038/s41388-017-0045-7.
6. Zhu, H., Acquaviva, J., Ramachandran, P., Boskovitz, A., Woolfenden, S., Pfannl, R., Bronson, R.T., Chen, J.W., Weissleder, R., Housman, D.E., and Charest, A. (2009). Oncogenic EGFR signaling cooperates with loss of tumor suppressor gene functions in gliomagenesis. Proc. Natl. Acad. Sci. USA *106*, 2712–2716. https://doi.org/10.1073/pnas.0813314106.
7. Jun, H.J., Acquaviva, J., Chi, D., Lessard, J., Zhu, H., Woolfenden, S., Bronson, R.T., Pfannl, R., White, F., Housman, D.E., et al. (2012). Acquired MET expression confers resistance to EGFR inhibition in a mouse model of glioblastoma multiforme. Oncogene *31*, 3039–3050. https://doi.org/10.1038/onc.2011.474.
8. Acquaviva, J., Jun, H.J., Lessard, J., Ruiz, R., Zhu, H., Donovan, M., Woolfenden, S., Boskovitz, A., Raval, A., Bronson, R.T., et al. (2011). Chronic activation of wild-type epidermal growth factor receptor and loss of Cdkn2a cause mouse glioblastoma formation. Cancer Res. *71*, 7198–7206. https://doi.org/10.1158/0008-5472.CAN-11-1514.
9. Yeo, A.T., Jun, H.J., Appleman, V.A., Zhang, P., Varma, H., Sarkaria, J.N., and Charest, A. (2021). EGFRvIII tumorigenicity requires PDGFRA co-signaling and reveals therapeutic vulnerabilities in glioblastoma. Oncogene *40*, 2682–2696. https://doi.org/10.1038/s41388-021-01721-9.
10. Lee, Y.R., Chen, M., and Pandolfi, P.P. (2018). The functions and regulation of the PTEN tumour suppressor: new modes and prospects. Nat. Rev. Mol. Cell Biol. *19*, 547–562. https://doi.org/10.1038/s41580-018-0015-0.
11. Song, M.S., Salmena, L., and Pandolfi, P.P. (2012). The functions and regulation of the PTEN tumour suppressor. Nat. Rev. Mol. Cell Biol. *13*, 283–296.
12. Manning, B.D., and Toker, A. (2017). AKT/PKB Signaling: Navigating the Network. Cell *169*, 381–405. https://doi.org/10.1016/j.cell.2017.04.001.
13. Trotman, L.C., Wang, X., Alimonti, A., Chen, Z., Teruya-Feldstein, J., Yang, H., Pavletich, N.P., Carver, B.S., Cordon-Cardo, C., Erdjument-Bromage, H., et al. (2007). Ubiquitination regulates PTEN nuclear import and tumor suppression. Cell *128*, 141–156. https://doi.org/10.1016/j.cell.2006.11.040.
14. Bassi, C., Ho, J., Srikumar, T., Dowling, R.J.O., Gorrini, C., Miller, S.J., Mak, T.W., Neel, B.G., Raught, B., and Stambolic, V. (2013). Nuclear PTEN controls DNA repair and sensitivity to genotoxic stress. Science *341*, 395–399. https://doi.org/10.1126/science.1236188.
15. Kuchay, S., Giorgi, C., Simoneschi, D., Pagan, J., Missiroli, S., Saraf, A., Florens, L., Washburn, M.P., Collazo-Lorduy, A., Castillo-Martin, M., et al. (2017). PTEN counteracts FBXL2 to promote IP3R3- and Ca(2+)-mediated apoptosis limiting tumour growth. Nature *546*, 554–558. https://doi.org/10.1038/nature22965.
16. Zhao, D., Lu, X., Wang, G., Lan, Z., Liao, W., Li, J., Liang, X., Chen, J.R., Shah, S., Shang, X., et al. (2017). Synthetic essentiality of chromatin remodelling factor CHD1 in PTEN-deficient cancer. Nature *542*, 484–488. https://doi.org/10.1038/nature21357.
17. Yehia, L., Keel, E., and Eng, C. (2020). The Clinical Spectrum of PTEN Mutations. Annu. Rev. Med. *71*, 103–116. https://doi.org/10.1146/annurev-med-052218-125823.
18. Papa, A., Wan, L., Bonora, M., Salmena, L., Song, M.S., Hobbs, R.M., Lunardi, A., Webster, K., Ng, C., Newton, R.H., et al. (2014). Cancer-associated PTEN mutants act in a dominant-negative manner to suppress PTEN protein function. Cell *157*, 595–610. https://doi.org/10.1016/j.cell.2014.03.027.
19. Zehir, A., Benayed, R., Shah, R.H., Syed, A., Middha, S., Kim, H.R., Srinivasan, P., Gao, J., Chakravarty, D., Devlin, S.M., et al. (2017). Mutational landscape of metastatic cancer revealed from prospective clinical sequencing of 10,000 patients. Nat. Med. *23*, 703–713. https://doi.org/10.1038/nm.4333.
20. Cancer Genome Atlas Research Network, Weinstein, J.N., Collisson, E.A., Mills, G.B., Shaw, K.R.M., Ozenberger, B.A., Ellrott, K., Shmulevich, I., Sander, C., and Stuart, J.M. (2013). The Cancer Genome Atlas Pan-Cancer analysis project. Nat. Genet. *45*, 1113–1120. https://doi.org/10.1038/ng.2764.
21. Tate, J.G., Bamford, S., Jubb, H.C., Sondka, Z., Beare, D.M., Bindal, N., Boutselakis, H., Cole, C.G., Creatore, C., Dawson, E., et al. (2019). COSMIC: the Catalogue Of Somatic Mutations In Cancer. Nucleic Acids Res. *47*, D941–D947. https://doi.org/10.1093/nar/gky1015.
22. Forbes, S.A., Beare, D., Boutselakis, H., Bamford, S., Bindal, N., Tate, J., Cole, C.G., Ward, S., Dawson, E., Ponting, L., et al. (2017). COSMIC: somatic cancer genetics at high-resolution. Nucleic Acids Res. *45*, D777–D783. https://doi.org/10.1093/nar/gkw1121.
23. Han, S.Y., Kato, H., Kato, S., Suzuki, T., Shibata, H., Ishii, S., Shiiba, K., Matsuno, S., Kanamaru, R., and Ishioka, C. (2000). Functional evaluation of PTEN missense mutations using in vitro phosphoinositide phosphatase assay. Cancer Res. *60*, 3147–3151.
24. Mighell, T.L., Evans-Dutson, S., and O'Roak, B.J. (2018). A Saturation Mutagenesis Approach to Understanding PTEN Lipid Phosphatase Activity and Genotype-Phenotype Relationships. Am. J. Hum. Genet. *102*, 943–955. https://doi.org/10.1016/j.ajhg.2018.03.018.
25. Myers, M.P., Pass, I., Batty, I.H., Van der Kaay, J., Stolarov, J.P., Hemmings, B.A., Wigler, M.H., Downes, C.P., and Tonks, N.K. (1998). The lipid phosphatase activity of PTEN is critical for its tumor supressor function. Proc. Natl. Acad. Sci. USA *95*, 13513–13518. https://doi.org/10.1073/pnas.95.23.13513.
26. Gildea, J.J., Herlevsen, M., Harding, M.A., Gulding, K.M., Moskaluk, C.A., Frierson, H.F., and Theodorescu, D. (2004). PTEN can inhibit in vitro organotypic and in vivo orthotopic invasion of human bladder cancer cells even in the absence of its lipid phosphatase activity. Oncogene *23*, 6788–6797. https://doi.org/10.1038/sj.onc.1207599.
27. Davidson, L., Maccario, H., Perera, N.M., Yang, X., Spinelli, L., Tibarewal, P., Glancy, B., Gray, A., Weijer, C.J., Downes, C.P., and Leslie, N.R. (2010). Suppression of cellular proliferation and invasion by the concerted lipid and protein phosphatase activities of PTEN. Oncogene *29*, 687–697. https://doi.org/10.1038/onc.2009.384.
28. Tibarewal, P., Zilidis, G., Spinelli, L., Schurch, N., Maccario, H., Gray, A., Perera, N.M., Davidson, L., Barton, G.J., and Leslie, N.R. (2012). PTEN protein phosphatase activity correlates with control of gene expression and invasion, a tumor-suppressing phenotype, but not with AKT activity. Sci. Signal. *5*, ra18. https://doi.org/10.1126/scisignal.2002138.
29. Kovacina, K.S., Park, G.Y., Bae, S.S., Guzzetta, A.W., Schaefer, E., Birnbaum, M.J., and Roth, R.A. (2003). Identification of a proline-rich Akt substrate as a 14-3-3 binding partner. J. Biol. Chem. *278*, 10189–10194. https://doi.org/10.1074/jbc.M210837200.
30. Thompson, A., Schäfer, J., Kuhn, K., Kienle, S., Schwarz, J., Schmidt, G., Neumann, T., Johnstone, R., Mohammed, A.K.A., and Hamon, C. (2003). Tandem mass tags: a novel quantification strategy for comparative analysis of complex protein mixtures by MS/MS. Anal. Chem. *75*, 1895–1904. https://doi.org/10.1021/ac0262560.
31. O'Connell, J.D., Paulo, J.A., O'Brien, J.J., and Gygi, S.P. (2018). Proteome-Wide Evaluation of Two Common Protein Quantification Methods. J. Proteome Res. *17*, 1934–1942. https://doi.org/10.1021/acs.jproteome.8b00016.
32. Johnson, J.L., Yaron, T.M., Huntsman, E.M., Kerelsky, A., Song, J., Regev, A., Lin, T.Y., Liberatore, K., Cizin, D.M., Cohen, B.M., et al. (2023). An atlas of substrate specificities for the human serine/threonine kinome. Nature *613*, 759–766. https://doi.org/10.1038/s41586-022-05575-3.
33. Ventura, A., Kirsch, D.G., McLaughlin, M.E., Tuveson, D.A., Grimm, J., Lintault, L., Newman, J., Reczek, E.E., Weissleder, R., and Jacks, T. (2007). Restoration of p53 function leads to tumour regression in vivo. Nature *445*, 661–665. https://doi.org/10.1038/nature05541.
34. Serrano, M., Lee, H., Chin, L., Cordon-Cardo, C., Beach, D., and DePinho, R.A. (1996). Role of the INK4a locus in tumor suppression and cell mortality. Cell *85*, 27–37. https://doi.org/10.1016/s0092-8674(00)81079-x.
35. Lesche, R., Groszer, M., Gao, J., Wang, Y., Messing, A., Sun, H., Liu, X., and Wu, H. (2002). Cre/loxP-mediated inactivation of the murine Pten tumor suppressor gene. genesis *32*, 148–149.
36. Woolfenden, S., Zhu, H., and Charest, A. (2009). A Cre/LoxP conditional luciferase reporter transgenic mouse for bioluminescence monitoring of tumorigenesis. Genesis *47*, 659–666. https://doi.org/10.1002/dvg.20545.
37. Yeo, A.T., Rawal, S., Delcuze, B., Christofides, A., Atayde, A., Strauss, L., Balaj, L., Rogers, V.A., Uhlmann, E.J., Varma, H., et al. (2022). Single-cell RNA sequencing reveals evolution of immune landscape during glioblastoma progression. Nat. Immunol. *23*, 971–984. https://doi.org/10.1038/s41590-022-01215-0.
38. Yeo, A.T., Shah, R., Aliazis, K., Pal, R., Xu, T., Zhang, P., Rawal, S., Rose, C.M., Varn, F.S., Appleman, V.A., et al. (2023). Driver Mutations Dictate the Immunologic Landscape and Response to Checkpoint

Immunotherapy of Glioblastoma. Cancer Immunol. Res. *11*, 629–645. https://doi.org/10.1158/2326-6066.CIR-22-0655.

39. Los, G.V., Encell, L.P., McDougall, M.G., Hartzell, D.D., Karassina, N., Zimprich, C., Wood, M.G., Learish, R., Ohana, R.F., Urh, M., et al. (2008). HaloTag: a novel protein labeling technology for cell imaging and protein analysis. ACS Chem. Biol. *3*, 373–382. https://doi.org/10.1021/cb800025k.
40. Rodriguez-Escudero, I., Oliver, M.D., Andres-Pons, A., Molina, M., Cid, V.J., and Pulido, R. (2011). A comprehensive functional analysis of PTEN mutations: implications in tumor- and autism-related syndromes. Hum. Mol. Genet. *20*, 4132–4142. https://doi.org/10.1093/hmg/ddr337.
41. Post, K.L., Belmadani, M., Ganguly, P., Meili, F., Dingwall, R., McDiarmid, T.A., Meyers, W.M., Herrington, C., Young, B.P., Callaghan, D.B., et al. (2020). Multi-model functionalization of disease-associated PTEN missense mutations identifies multiple molecular mechanisms underlying protein dysfunction. Nat. Commun. *11*, 2073. https://doi.org/10.1038/s41467-020-15943-0.
42. Hasle, N., Matreyek, K.A., and Fowler, D.M. (2019). The Impact of Genetic Variants on PTEN Molecular Functions and Cellular Phenotypes. Cold Spring Harb. Perspect. Med. *9*, a036228. https://doi.org/10.1101/cshperspect.a036228.
43. Masson, G.R., and Williams, R.L. (2020). Structural Mechanisms of PTEN Regulation. Cold Spring Harb. Perspect. Med. *10*, a036152. https://doi.org/10.1101/cshperspect.a036152.
44. Naguib, A., Bencze, G., Cho, H., Zheng, W., Tocilj, A., Elkayam, E., Faehnle, C.R., Jaber, N., Pratt, C.P., Chen, M., et al. (2015). PTEN functions by recruitment to cytoplasmic vesicles. Mol. Cell *58*, 255–268. https://doi.org/10.1016/j.molcel.2015.03.011.
45. Choi, S.W., Lee, Y., Shin, K., Koo, H., Kim, D., Sa, J.K., Cho, H.J., Shin, H.M., Lee, S.J., Kim, H., et al. (2021). Mutation-specific non-canonical pathway of PTEN as a distinct therapeutic target for glioblastoma. Cell Death Dis. *12*, 374. https://doi.org/10.1038/s41419-021-03657-0.
46. Yang, J.M., Nguyen, H.N., Sesaki, H., Devreotes, P.N., and Iijima, M. (2015). Engineering PTEN function: membrane association and activity. Methods *77–78*, 119–124. https://doi.org/10.1016/j.ymeth.2014.10.018.
47. Nguyen, H.N., Yang, J.M., Jr., Rahdar, M., Keniry, M., Swaney, K.F., Parsons, R., Park, B.H., Sesaki, H., Devreotes, P.N., and Iijima, M. (2015). A new class of cancer-associated PTEN mutations defined by membrane translocation defects. Oncogene *34*, 3737–3743. https://doi.org/10.1038/onc.2014.293.
48. Nguyen, H.N., Yang, J.M., Miyamoto, T., Itoh, K., Rho, E., Zhang, Q., Inoue, T., Devreotes, P.N., Sesaki, H., and Iijima, M. (2015). Opening the conformation is a master switch for the dual localization and phosphatase activity of PTEN. Sci. Rep. *5*, 12600. https://doi.org/10.1038/srep12600.
49. Wei, Y., Stec, B., Redfield, A.G., Weerapana, E., and Roberts, M.F. (2015). Phospholipid-binding sites of phosphatase and tensin homolog (PTEN): exploring the mechanism of phosphatidylinositol 4,5-bisphosphate activation. J. Biol. Chem. *290*, 1592–1606. https://doi.org/10.1074/jbc.M114.588590.
50. Schultz, D.F., Billadeau, D.D., and Jois, S.D. (2023). EGFR trafficking: effect of dimerization, dynamics, and mutation. Front. Oncol. *13*, 1258371. https://doi.org/10.3389/fonc.2023.1258371.
51. Salmena, L., Carracedo, A., and Pandolfi, P.P. (2008). Tenets of PTEN tumor suppression. Cell *133*, 403–414. https://doi.org/10.1016/j.cell.2008.04.013.
52. Heinrich, F., Chakravarthy, S., Nanda, H., Papa, A., Pandolfi, P.P., Ross, A.H., Harishchandra, R.K., Gericke, A., and Lösche, M. (2015). The PTEN Tumor Suppressor Forms Homodimers in Solution. Structure *23*, 1952–1957. https://doi.org/10.1016/j.str.2015.07.012.
53. Perez-Riverol, Y., Bai, J., Bandla, C., García-Seisdedos, D., Hewapathirana, S., Kamatchinathan, S., Kundu, D.J., Prakash, A., Frericks-Zipper, A., Eisenacher, M., et al. (2022). The PRIDE database resources in 2022: a hub for mass spectrometry-based proteomics evidences. Nucleic Acids Res. *50*, D543–D552. https://doi.org/10.1093/nar/gkab1038.
54. Shin, K.J., Wall, E.A., Zavzavadjian, J.R., Santat, L.A., Liu, J., Hwang, J.I., Rebres, R., Roach, T., Seaman, W., Simon, M.I., and Fraser, I.D.C. (2006). A single lentiviral vector platform for microRNA-based conditional RNA interference and coordinated transgene expression. Proc. Natl. Acad. Sci. USA *103*, 13759–13764. https://doi.org/10.1073/pnas.0606179103.
55. Jun, H.J., Appleman, V.A., Wu, H.J., Rose, C.M., Pineda, J.J., Yeo, A.T., Delcuze, B., Lee, C., Gyuris, A., Zhu, H., et al. (2018). A PDGFRalpha-driven mouse model of glioblastoma reveals a stathmin1-mediated mechanism of sensitivity to vinblastine. Nat. Commun. *9*, 3116. https://doi.org/10.1038/s41467-018-05036-4.
56. Madisen, L., Zwingman, T.A., Sunkin, S.M., Oh, S.W., Zariwala, H.A., Gu, H., Ng, L.L., Palmiter, R.D., Hawrylycz, M.J., Jones, A.R., et al. (2010). A robust and high-throughput Cre reporting and characterization system for the whole mouse brain. Nat. Neurosci. *13*, 133–140. https://doi.org/10.1038/nn.2467.
57. Lonic, A., Onglao, W., and Khew-Goodall, Y. (2022). Quantifying EGFR endosomal recycling via immunofluorescence in breast cancer cells. STAR Protoc. *3*, 101305. https://doi.org/10.1016/j.xpro.2022.101305.
58. Li, J., Cai, Z., Bomgarden, R.D., Pike, I., Kuhn, K., Rogers, J.C., Roberts, T.M., Gygi, S.P., and Paulo, J.A. (2021). TMTpro-18plex: The Expanded and Complete Set of TMTpro Reagents for Sample Multiplexing. J. Proteome Res. *20*, 2964–2972. https://doi.org/10.1021/acs.jproteome.1c00168.
59. Paulo, J.A., Navarrete-Perea, J., Erickson, A.R., Knott, J., and Gygi, S.P. (2018). An Internal Standard for Assessing Phosphopeptide Recovery from Metal Ion/Oxide Enrichment Strategies. J. Am. Soc. Mass Spectrom. *29*, 1505–1511. https://doi.org/10.1007/s13361-018-1946-6.
60. Ting, L., Rad, R., Gygi, S.P., and Haas, W. (2011). MS3 eliminates ratio distortion in isobaric multiplexed quantitative proteomics. Nat. Methods *8*, 937–940. https://doi.org/10.1038/nmeth.1714.
61. Chambers, M.C., Maclean, B., Burke, R., Amodei, D., Ruderman, D.L., Neumann, S., Gatto, L., Fischer, B., Pratt, B., Egertson, J., et al. (2012). A cross-platform toolkit for mass spectrometry and proteomics. Nat. Biotechnol. *30*, 918–920. https://doi.org/10.1038/nbt.2377.
62. Beausoleil, S.A., Villén, J., Gerber, S.A., Rush, J., and Gygi, S.P. (2006). A probability-based approach for high-throughput protein phosphorylation analysis and site localization. Nat. Biotechnol. *24*, 1285–1292. https://doi.org/10.1038/nbt1240.
63. Huttlin, E.L., Jedrychowski, M.P., Elias, J.E., Goswami, T., Rad, R., Beausoleil, S.A., Villén, J., Haas, W., Sowa, M.E., and Gygi, S.P. (2010). A tissue-specific atlas of mouse protein phosphorylation and expression. Cell *143*, 1174–1189. https://doi.org/10.1016/j.cell.2010.12.001.
64. Elias, J.E., and Gygi, S.P. (2010). Target-decoy search strategy for mass spectrometry-based proteomics. Methods Mol. Biol. *604*, 55–71. https://doi.org/10.1007/978-1-60761-444-9_5.
65. Elias, J.E., and Gygi, S.P. (2007). Target-decoy search strategy for increased confidence in large-scale protein identifications by mass spectrometry. Nat. Methods *4*, 207–214. https://doi.org/10.1038/nmeth1019.
66. McAlister, G.C., Huttlin, E.L., Haas, W., Ting, L., Jedrychowski, M.P., Rogers, J.C., Kuhn, K., Pike, I., Grothe, R.A., Blethrow, J.D., and Gygi, S.P. (2012). Increasing the multiplexing capacity of TMTs using reporter ion isotopologues with isobaric masses. Anal. Chem. *84*, 7469–7478. https://doi.org/10.1021/ac301572t.
67. Ritchie, M.E., Phipson, B., Wu, D., Hu, Y., Law, C.W., Shi, W., and Smyth, G.K. (2015). limma powers differential expression analyses for RNA-sequencing and microarray studies. Nucleic Acids Res. *43*, e47. https://doi.org/10.1093/nar/gkv007.

STAR★METHODS

KEY RESOURCES TABLE

REAGENT or RESOURCE	SOURCE	IDENTIFIER
Antibodies		
anti-EGFR	Zymed	28–0005
anti-PTEN	Cell Signaling Technology	9559
anti-EGFR-tyr845	Cell Signaling Technology	2231
anti-EGFR-tyr992	Cell Signaling Technology	2235
anti-EGFR-tyr1045	Cell Signaling Technology	2237
anti-EGFR-tyr1068	Cell Signaling Technology	3777
anti-EGFR-tyr1086	Cell Signaling Technology	2220
anti-EGFR-tyr1148	Cell Signaling Technology	4404
anti-EGFR-tyr1173	Cell Signaling Technology	4407
anti-EGFR	Cell Signaling Technology	2232
anti-b-actin	Cell Signaling Technology	3700
anti-pan-cadherin	Cell Signaling Technology	4068
anti-laminB1	Cell Signaling Technology	13435
anti-GAPDH	Cell Signaling Technology	5174
anti-AKT-Ser-473	Cell Signaling Technology	9217
anti-AKT-Thr-308	Cell Signaling Technology	9275
anti-AKT	Cell Signaling Technology	9272
anti-S6 ribosomal protein-Ser-235/236	Cell Signaling Technology	4858
anti-S6 ribosomal protein-Ser-240/244	Cell Signaling Technology	5364
anti-S6 ribosomal protein	Cell Signaling Technology	2217
anti-MEK1/2-Ser-217/221	Cell Signaling Technology	9154
anti-MEK1/2	Cell Signaling Technology	9126
anti-p44/42 ERK1/2-Thr202/Tyr204	Cell Signaling Technology	4370
anti-p44/42 ERK1/2	Cell Signaling Technology	4695
anti-STAT3-Tyr-705	Cell Signaling Technology	9145
anti-STAT3	Cell Signaling Technology	12640
anti-STAT3-Ser-727	Cell Signaling Technology	9134
anti-AKT1-Ser-473	Cell Signaling Technology	9018
anti-AKT1	Cell Signaling Technology	2938
anti-AKT2Ser-474	Cell Signaling Technology	8599
anti-AKT2	Cell Signaling Technology	3063
anti-PRAS40-Thr-246	Cell Signaling Technology	2997
anti-PRAS40	Cell Signaling Technology	2691
anti-PTEN	Invitrogen	MA5-12278
anti-GFPA	Dako	Z0334
anti-NEU	Thermo Fisher	MA5-33103
anti-EGFR Ab3	Millipore Sigma	GR13
Alexa 488-conjugated anti-PTEN	R&D systems	IC847G
Bacterial and virus strains		
pSLIK-PTEN	This study	

(*Continued on next page*)

Continued

REAGENT or RESOURCE	SOURCE	IDENTIFIER
Chemicals, peptides, and recombinant proteins		
Fugene6	Promega	E2691
Antibiotic Puromycin	Thermo Fisher	A1113803
Antibiotic Blasticidin	Thermo Fisher	A1113902
Critical commercial assays		
PIP3 Mass ELISA kit	Echelon	K-2500s
HaloLINK resin	Promega	G1912
Deposited data		
Proteomics data	proteomexchange.org	PXD051485
Experimental models: Cell lines		
Mouse primary astrocytes	This study	
Experimental models: Organisms/strains		
LSL-EGFRvIII; Cdkn2a−/−;PTEN2lox/2lox,LSL-Luc	This study	
Oligonucleotides		
human PTEN; forward CCAGAGACAAAAAGGG AGTAACT reverse ATGAACTTGTCTTCCCGTCGT	This study	
mouse b-actin forward GGAGAAGAGCTACGA GCTGCCTGAC reverse AAGGTAGTT TCGTGGATGCCACAGG	This study	
Recombinant DNA		
pSLIK-PTEN	This study	
pSLIK-HALO-PTEN	This study	
pSLIK-PTEN-HALO	This study	
Software and algorithms		
GraphPad Prism	GraphPad	
Zen Blue	Zeiss	
MSconvert	ProteoWizard	
Image Studio	Licor	
In vivo Imaging Software	Revvity	
FlowJo	FlowJo	
Illustrator	Adobe	
CellSens Entry	Olympus	
Limma v3.42	R	

EXPERIMENTAL MODEL AND STUDY PARTICIPANT DETAILS

EGFR^{VIII} conditional mice and primary astrocyte cell cultures

All mouse procedures were performed in accordance with Beth Israel Deaconess Medical Center recommendations for care and use of animals and were maintained and handled under protocols approved by the Institutional Animal Care and Use Committee. The Cre/Lox-mediated conditional expression of the human EGFR^{VIII} (LSL-EGFR^{vIII};Cdkn2a$^{-/-}$;PTEN^{2lox}) was described elsewhere.[6–9] Primary mouse astrocytes isolated from P0-P1 LSL-EGFR^{vIII};Cdkn2a$^{-/-}$;PTEN^{2lox} neonate mice were established. Briefly, brains were isolated and meninges and brainstems were carefully removed. Resulting cortices were minced in 0.25% trypsin (w/v), 1mM EDTA, and allowed to disaggregate for 15 min at 37°C. The cell suspension was strained through a 70μm cell strainer (Falcon). Cells were washed in PBS three times and plated on 0.2% gelatin-coated tissue culture plates and then cultured in Dulbecco's modified Eagle's medium (DMEM) supplemented with 10% (v/v) heat inactivated fetal bovine serum (FBS) and antibiotics.

Intracranial stereotactic injections

Adult animals (12 weeks of age and older) of the indicated genotype were anesthetized with an IP injection of ketamine/xylazine (ketamine 100–125 mg/kg, xylazine 10–12.5 mg/kg). The animals were mounted in a Stoelting stereotaxic frame (Harvard Apparatus Inc.) with nonpuncturing ear bars. The incision site was shaved and sterilized with betadine surgical scrub, and a single incision was made from the anterior pole of the skull to the posterior ridge. A 1-mm burr hole was drilled at the stereotactically defined location of the striatum (2.1 mm rostral to the bregma, 1.5 mm lateral to the midline, and at 2 mm depth to the pia surface) and either a 1μL Hamilton syringe or a pulled glass pipette mounted onto a Nanoject II injector (Drummond Scientific Company) was used to inject either adeno-CMV Cre virus (Gene Transfer Vector Core, University of Iowa, Iowa City, IA) or the indicated DOX-inducible lentivirus at a rate of 0.1 μL/min. Following retraction of the syringe or pipette, the burr hole was filled with sterile bone wax, the skin drawn up and sutured, and the animal placed in a cage with a padded bottom atop a surgical heat pad until ambulatory.

Bioluminescence

Imaging bioluminescence was measured using the IVIS 200 imaging system (Xenogen). All of the images were taken 10 min after IP injection of luciferin (225 mg/kg, Xenogen) suspended in sterile phosphate-buffered saline to allow proper distribution of luciferin, with a 60-s photon acquisition during which mice were subjected to inhalational of 3% isoflurane anesthesia. All image analyses and bioluminescent quantification were performed using Living Image software v. 2.50 (Xenogen).

Tumor growth in immunocompromised mice

1×10^6 of the indicated cells were mixed with Matrigel and injected subcutaneously in the flanks of 6 weeks athymic nude ($Ncr^{Nu/Nu}$) mice and tumors were measured every three days using a caliper. Tumor volume was calculated length × $width^2$ × 0.5. Comparison of tumor volumes from allelic series were performed on day 30 once tumors from control cells had reached maximal tolerated size. Doxycycline (DOX) treatment (DOX diet of 625 mg/kg) was initiated as indicated.

METHOD DETAILS

Histology and immunohistochemistry

Deeply anesthetized animals were transcardially perfused with cold PBS. Brains were excised, rinsed in PBS, and serial coronal sections cut using a brain mold and postfixed in 4% (w/v) paraformaldehyde overnight. Formalin-fixed tissues were embedded in paraffin, sectioned at 5–10 μm, and stained with H&E (Sigma, St. Louis, MO, USA) for histopathological analysis. For immunohistochemistry (IHC), cut sections were deparaffinized and rehydrated through xylenes and graded alcohol series and rinsed for 5 min under tap water. Antigen target retrieval solution (Dako, S1699, Santa Clara, CA, USA) was used to unmask the antigen (microwave for 10 min at low power then cooled down for 30 min) followed by 3 washes with PBS for 5 min each. Quenching of endogenous peroxidase activity was performed by incubating the sections for 10 min in 0.3% H_2O_2 in methanol followed by PBS washes. Slides were preincubated in blocking solution [5% (v/v) goat serum (Sigma) in PBS 0.3% (v/v) Triton X-100] for 1 h at room temperature, followed by mouse-on-mouse blocking reagent (Vector Labs, Inc.; MKB-2213) incubation for 1 h. Primary antibody was incubated for 24 h at 4°C. Secondary antibodies used were biotinylated anti-rabbit or anti-mouse (1:500, Vector Labs, Inc.; Burlingame, CA, USA) for IHC and were incubated for 1 h at room temperature. All antibodies were diluted in blocking solution. All immunobinding of primary antibodies was detected by biotin-conjugated secondary antibodies and Vectastain ABC kit (Vector Labs, Inc.) using DAB (Vector Labs, Inc.) as a substrate for peroxidase and counterstained with hematoxylin. The following primary antibodies were used: EGFR (28-0005, 1:200, Zymed, South San Francisco, CA, USA), and rabbit mAb PTEN (Cell Signaling Technology, #9559; 1:200).

Soft agar assay

Adherence-independent growth was studied by plating 10^2 cells of each PTEN mutant astrocyte cell lines in 0.6% (w/v) semi-solid soft agarose mixed with DMEM and supplemented with 10% FBS in a 6 well plate. Fresh medium was added every 3 days in a 10 μg/mL (w/v) Doxycycline (DOX) and colonies were microscopically visualized after 21 days.

Immunoblot

Cell lysates were prepared using radioimmunoprecipitation (RIPA) buffer supplemented with 5 mM Na_3VO_4 (freshly made) and Complete (Roche) protease inhibitor cocktail. Equi-amount of total cell lysates were separated by SDS-PAGE and electrotransfered to polyvinylidene fluoride (PVDF) membrane (Immobilon P; Millipore). Blots were blocked in Odyssey Blocking Buffer (TBS, LiCOR) for 1 h at room temperature on a shaker. Primary antibodies were added to blocking solution and incubated overnight at 4°C on a shaker. Blots were washed three times with TBS-T, and secondary antibodies (IRDye 800CW Goat anti-Rabbit or IRDye 680RD Goat anti-Mouse, LiCOR) were added at 1:5,000 dilution into blocking solution with 0.2% (v/v) Tween 20 and 0.01% (w/v) SDS and incubated for 1 h at room temperature on a shaker in the dark. After three TBS-T washes, blots were then imaged using an Odyssey LiCOR Imaging System, and quantification was performed with Image Studio Lite Image Analysis Software. The primary antibodies used in these studies are: The following primary antibodies used in these studies were obtained from Cell Signaling Technology: *p*-EGFR (Tyr-845; Rabbit, 1:1,000, 2231), *p*-EGFR (Tyr-992; Rabbit, 1:1,000, 2235), *p*-EGFR (Tyr-1045; Rabbit, 1:1,000, 2237), *p*-EGFR (Tyr-1068; Rabbit, 1:1,000, 3777), *p*-EGFR (Tyr-1086; Rabbit, 1:1,000, 2220), *p*-EGFR

(Tyr-1148; Rabbit, 1:1,000, 4404), *p*-EGFR (Tyr-1173; Rabbit, 1:1,000, 4407), EGFR (Rabbit, 1:1,000, 2232), PTEN (Rabbit, 1:1,000, 9559), β-Actin (Mouse, 1:2,000, 3700), pan-Cadherin (Rabbit, 1:1,000, 4068), Lamin B1 (Rabbit, 1:1,000, 13435), GAPDH (Rabbit, 1:1,000, 5174), *p*-AKT (Ser-473; Rabbit, 1:1,000, 9217), *p*-AKT (Thr-308; Rabbit, 1:1,000, 9275), AKT (Rabbit, 1:1,000, 9272), p-S6 Ribosomal Protein (Ser-235/236; Rabbit, 1:1,000, 4858), p-S6 Ribosomal Protein (Ser-240/244; Rabbit, 1:1,000, 5364), S6 Ribosomal Protein (Rabbit, 1:1,000, 2217), *p*-MEK1/2 (Ser-217/221; Rabbit, 1:1,000, 9154), p-p44/p42 ERK (Rabbit, 1:1,000, 9126), p-p44/p42 ERK (Thr-202/Tyr-204; Rabbit, 1:1,000, 4370), p-p44/p42 ERK (Rabbit, 1:1,000, 4695), p-STAT3 (Tyr-705; Rabbit, 1:1,000, 9145), p-STAT3 (Ser-727; Rabbit, 1:1,000, 9134), STAT3 (Rabbit, 1:1,000, 12640), *p*-AKT1 (Ser-473; Rabbit, 1:1,000, 9018), AKT1 (Rabbit, 1:1,000, 2938), *p*-AKT2 (Ser-474; Rabbit, 1:1,000, 8599), AKT2 (Rabbit, 1:1,000, 3063), *p*-PRAS40 (Thr-246; Rabbit, 1:1,000, 2997), PRAS40 (Rabbit, 1:1,000, 2691).

PTEN mutants, HaloTag fusion and virus construct design, production and titer determination

Missense mutant PTEN cDNAs were constructed as follows: a wild type human PTEN cDNA was cloned downstream of a tetracycline response element (TRE) promotor into the pEntry vector and subjected to site directed mutagenesis using Quickchange Mutagenesis Kit (Stratagene) according to the manufacturer's protocol. All constructs were sequenced for sequence accuracy validation. The TRE-PTEN cDNAs were transferred to the pSLIK (single lentivector for inducible knock-down) lentivirus vector system[54] modified to express Cre recombinase or blasticidine selection gene.[55] Briefly, the modification of the original lentiviral vector platform supports constitutive expression of a Tet-transactivating component (rtTa3) under a Ubc promoter and the cDNA for Cre recombinase or Blasticidine resistance gene through an Internal Ribosomal Entry Site (IRES) and inducible PTEN cDNAs expression under doxycycline (DOX) treatments. HaloTag sequence was introduced into the pSLIK PTEN vectors using basic molecular cloning techniques. Viruses were produced by co-transfection of 293T cells with packaging vectors and purified by ultracentrifugation of conditioned media, resuspended in PBS, aliquoted in single use amounts and stored at −80°C. To standardize intracranial injections with identical viral titers, viral preparations were functionally titered for Cre activity by serial dilution infection of immortalized fibroblasts derived from Cdkn2a-null conditional LSL-tdTomato Ai9 reporter mouse strain.[56] For *in vitro* work, fresh viruses were used to infect $EGFR^{vIII}$;$Cdkn2a^{-/-}$;$PTEN^{lox/lox}$ astrocytes and single clones were isolated post blasticidine selection for analysis. 3–5 clones of each PTEN missense mutants were selected and used in the studies.

Immunofluorescence

Cells were placed on chamber slides into medium (10% (w/v) Heat Inactivated FBS in DMEM) overnight, and where indicated, treated with 10 μg/mL of Doxycycline. After 48 h, cells were washed three times in PBS, fixed with freshly made 4% (w/v) paraformaldehyde for 10 min and permeabilized Triton X-100 (0.1% v/v) for 15 min at room temperature. The fixed and permeabilized cells were then blocked with PBS-T plus 10% (v/v) goat serum (Sigma) for 20 min at room temperature, followed by an incubation with primary antibody overnight at 4°C in a humidified chamber with blocking solution. After PBS washes, cells were incubated in FITC- conjugated goat anti-mouse IgG (1:500, Millipore) and Cy3-conjugated goat anti-rabbit secondary antibodies (1:1,000, Millipore) in blocking solution for 1 h at room temperature and washed in PBS. Fluorescence-stained slides were mounted with DAPI Slowfade Gold Antifade mounting media (Thermo Fisher). Images were acquired using a Zeiss LSM 880 Confocal Laser Scanning Microscope, and were analyzed and quantified using Zen Blue. The following antibodies were used: anti-PTEN antibody (Invitrogen MA5-12278) diluted 1:100, glial fibrillary acidic protein (GFAP; Dako Z0334) and NeuN (Thermo Fisher MA5-33103) diluted 1:500.

EGFR trafficking

Visualization and quantification of trafficking of plasma membrane EGFR was performed according to.[57] Briefly, Lab-tek II 4-well chamber slides (Thermo Fisher 177402) were coated with 350μL fibronectin (Millipore Sigma F1056) at 0.1 mg/mL for 30 min at 37°C. The fibronectin was aspirated and the plates were allowed to dry at room temperature uncovered inside the biosafety cabinet for 4 h 25,000 cells were counted and seeded on the dried chamber slides into medium (10% (w/v) Heat Inactivated FBS in DMEM and 10 μg/mL of Doxycycline) for 12 h, then starved in 0.1% (w/v) Heat Inactivated FBS in DMEM with 10 μg/mL of Doxycycline for 24 h. The chambers were put on ice. Where appropriate (baseline condition), cells were stripped immediately in ice-cold Stripping Solution (0.5 M acetic acid/0.2 M NaCl) for 2 × 1 min with moderate rocking. The acid strip solution was rigorously removed by washing 4 × 1 min with ice-cold Trafficking Solution (DMEM 0.1% FBS (w/v)), and fixed in Fixation Solution (3.7% formaldehyde in DMEM for 15 min on ice, followed by 10 min at room temperature). Cells to be studied for EGFR trafficking were placed in ice-cold Labeling Solution (DMEM, FBS 0.1% (w/v), 200 μg/mL anti-EGFR Ab-3 (Millipore Sigma GR13)) and rocked for 1 h on ice. Following EGFR surface labeling, cells to be analyzed at baseline were washed 4 × 1 min with ice-cold PBS and treated with Fixation Solution. Remaining chambers (internalization condition) were washed 4 × 1 min with ice-cold PBS, media replaced with 37°C Trafficking Solution, and pulsed in a 37°C incubator for 1 h. Cells were then washed 4 × 1 min with ice-cold PBS, washed 2 × 1 min with ice-cold Stripping Solution, all acid strip again carefully removed with 4 × 1 min wash in ice-cold Trafficking Solution, and fixed in Fixation Solution. All Fixation Solution was then removed, and the cells were washed 5 × 1 min in PBS with rocking. 400μL Block Solution (TBS 1x, Triton 0.1%, BSA 2%) was added and rocked at room temperature for 60 min. Block Solution was aspirated, and 400μL Secondary Antibody Solution (goat anti-mouse-Alexa Fluor 488 (Thermo Fisher A28175)) was added and rocked at room temperature for 60 min. The Secondary Antibody Solution was removed and washed 5 × 3 min in Wash Buffer (TBS 1x, Triton 0.1%), cells were mounted in ProLong Gold Antifade Mountant (Thermo Fisher P36934), and imaged using a Zeiss LSM 880 Confocal Laser Scanning Microscope. Images were analyzed and quantified in Zen Blue.

Flow cytometry

Intracellular levels of PTEN were measured by flow cytometry. Briefly, vehicle and 10 μg/mL Doxycycline treated cells for 48 h were trypsinized, collected by centrifugation and fixed in 4% (w/v) paraformaldehyde for 10 min at room temperature. Cells were permeabilized by resuspending in Tween 20 (0.05% v/v) and Saponin (0.05% v/v) for 20 min. The cells were then washed three times with PBS containing 0.5% BSA. A 1:11 dilution of Alexa Fluor 488 conjugated PTEN antibody (Miltenyi Biotech) was added to each assay tube and incubated for 1 h at room temperature. Cells were washed three times with PBS +0.5% (w/v) BSA and resuspended in 1mL PBS and analyzed by flow cytometry on a Beckman Gallios flow cytometer and using FlowJo software (TreeStar).

Cellular fractionation

Cells were trypsinized, washed with PBS and centrifuged at 500g for 3 min and the supernatant was discarded. Subcellular fractionation was then performed with the Subcellular Protein Fraction Kit for Cultured Cells (Thermo Fisher Scientific), according to the manufacturer's instructions.

Quantitative reverse transcriptase polymerase chain reaction

Total RNA was isolated using the RNeasy Mini Kit (Qiagen) in biological triplicates. cDNA was synthesized with a Superscript III First-strand Synthesis Supermix for quantitative reverse transcriptase polymerase chain reaction (qRT-PCR) kit (Thermo Fisher) according to the manufacturer's protocol. Expression was then analyzed using SYBR Green Real-Time PCR with human PTEN for (CCAGAGACAAAAAGGGAGTAACT) and PTEN rev (ATGAACTTGTCTTCCCGTCGT) primers for the detection of Human PTEN and mouse β-actin for (GGAGAAGAGCTAC GAGCTGCCTGAC) and mouse β-actin rev (AAGGTAGTTTCGTGGATGCCACAGG) primers for the detection of Mouse β-actin.

Cellular PIP3 analysis

Cells were plated at a density of 1 × 10^6 cells/10 cm dish in medium 10% (w/v) Heat Inactivated FBS in DMEM overnight, and treated with 10 μg/mL of Doxycycline. After 48 h, the medium was removed by gentle aspiration and immediately added 10 mL of ice-cold 0.5 M TCA. Cells were scraped, transferred into a 15 mL tube on ice, and centrifuged at 3,000 rpm for 7 min at 4°C. The pellet was resuspended in 3 mL of 5% tricarboxylic acid/1 μM EDTA, vortexed, and centrifuged at 3,000 rpm for 5 min, the supernatant was discarded, and this washing step was repeated one more time. Neutral lipids were extracted adding 3 mL of MeOH:$CHCl_3$ (2:1) (v/v) and vortexed for 10 min at room temperature. Extracts were centrifuged at 3,000 rpm for 5 min, the supernatant was discarded, and this extraction step was repeated one more time. The acidic lipids were extracted adding 2.25 mL MeOH:$CHCl_3$:12 M HCl (80:40:1) (v/v) with vortexing for 25 min at room temperature. Extracts were centrifuged at 3,000 rpm for 5 min and the supernatant was transferred to a new 15 mL tube; 0.75 mL of $CHCl_3$ and 1.35 mL of 0.1 M HCl were added to the supernatant, vortexed for 30 s, and centrifuged at 3,000 rpm for 5 min to separate organic and aqueous phases. The organic (lower) phase was collected; 1.5 mL were transferred into new vial for PIP_3 measurement. All samples were dried in a vacuum dryer for 1 h. PIP_3 samples were resuspended in 185 μL of PBS+ 0.25% Protein Stabilizer provided by the Echelon kit and sonicated in an ice-water bath for 10 min, vortexed, and spun down before adding to the ELISA. All experiments were performed in biological triplicate. Once phospholipids were isolated from cells, cellular PIP_3 concentrations were measured using a PIP3 Mass ELISA kit (Echelon, K-2500s) according to the manufacturer's instructions.

HaloTag PTEN fusion proteins

EGFRvIII; Cdkn2a−/−;PTEN2lox/2lox astrocytes were infected with HaloTag-PTEN and PTEN-HaloTag viruses and clones selected with blasticidine. Expression of HaloTag-PTEN and PTEN-HaloTag was achieve by incubating the cells with DOX (10 mg/mL) for 24 h. Proteins were extracted and affinity purified using Promega's HaloLink resin system according to the manufacturer protocol and affinity selected proteins were stripped off the beads using 8 M urea. Proteins were precipitated by methanol chloroform method and subjected to TMT LC-MS described below.

Proteomics and phosphoproteomics

Tandem mass tag labeling

TMTpro reagents[58] (0.8 mg) were dissolved in anhydrous acetonitrile (40 μL) of which 5 μL was added to the peptides (50 μg) with 15 μL of acetonitrile to achieve a final concentration of approximately 30% (v/v). Following incubation at room temperature for 1 h, the reaction was quenched with hydroxylamine to a final concentration of 0.3% (v/v). TMT-labeled samples were pooled at a 1:1 ratio across all samples. For each experiment, the pooled sample was vacuum centrifuged to near dryness and subjected to C18 solid-phase extraction (SPE) (Sep-Pak, Waters).

Spin column-based phosphopeptide enrichment

Phosphopeptides were enriched from this pooled sample using the High-Select Fe-NTA Phosphopeptide Enrichment Kit.[59] The only deviation from the manufacturer's protocol was that we prepared an "elution collection tube" with 100 μL of 10% formic acid into which the eluates

were eluted. The combined eluate was vacuum centrifuged to near dryness and desalted via StageTip. The unbound and wash was used for Offline basic pH reversed-phase BPRP fractionation to profile the proteome as described below.

Offline basic pH reversed-phase (BPRP) fractionation (whole proteome)

We fractionated the pooled TMT-labeled peptide sample (the unbound and wash from the phosphopeptide enrichment) via BPRP HPLC with an Agilent 1260 pump. Peptides were subjected to a 50 min linear gradient from 5% to 35% acetonitrile in 10 mM ammonium bicarbonate pH 8 at a flow rate of 0.8 mL/min over an Agilent 300Extend C18 column (5 μm particles, 4.6 mm ID and 22 cm long). The peptide mixture was fractionated into a total of 96 fractions, which were consolidated into 24 super-fractions, from which 12 non-adjacent samples were analyzed by mass spectrometry. These fractions were subsequently acidified with 1% formic acid and vacuum centrifuged to near dryness. Each fraction was also desalted via StageTip, dried via vacuum centrifugation, and reconstituted in 5% acetonitrile, 5% formic acid for LC-MS/MS processing.

Liquid chromatography and tandem mass spectrometry (whole proteome)

Our mass spectrometry data were collected using an Orbitrap Eclipse mass spectrometer (Thermo Fisher Scientific, San Jose, CA) coupled to a Thermo Vanquish *Neo* liquid chromatography (LC) system (Thermo Fisher Scientific). Peptides were separated on a 100 μm inner diameter microcapillary column packed with ~35 cm of Accucore150 resin (2.6 μm, 150 Å, ThermoFisher Scientific, San Jose, CA). For each analysis, we loaded ~1 μg onto the column. For protein level analysis, peptides were separated using a 90 min gradient of 3–24% acetonitrile in 0.125% formic acid at a flow rate of ~400 nL/min. Each analysis used the multi-notch MS3-based TMT method on an Orbitrap Fusion mass spectrometer. The scan sequence began with an MS1 spectrum (Orbitrap analysis; resolution 120,000; mass range 350–1400 m/z; automatic gain control (AGC) target 4.0E5; maximum injection time 50 ms). Precursors for MS2/MS3 analysis were selected using a Top10 method. Precursors were then selected for MS2/MS3 analysis.[60] MS2 analysis consisted of collision-induced dissociation (quadrupole ion trap analysis with turbo scan rate; AGC 1E4; normalized collision energy (NCE) 35; maximum injection time 60ms). MS3 precursors were fragmented by high energy collision-induced dissociation (HCD) and analyzed using the Orbitrap (NCE 65; AGC 1.5E5; maximum injection time 150 ms, resolution was 50,000).

Liquid chromatography and mass spectrometry data acquisition (whole proteome)

Mass spectrometry data were collected using a Orbitrap Eclipse mass spectrometer (Thermo Fisher Scientific, San Jose, CA) coupled with *Neo* Vanquish liquid chromatograph. Peptides were separated on a 100 μm inner diameter microcapillary column packed with ~20 cm of Accucore C18 resin (2.6 μm, 150 Å, Thermo Fisher Scientific). For each analysis, we loaded ~2 μg onto the column. Peptides were separated using a 90 min gradient of 5–29% acetonitrile in 0.125% formic acid with a flow rate of 300 μL/min. The scan sequence began with an Orbitrap MS^1 spectrum with the following parameters: resolution 60K, scan range 350–1350, automatic gain control (AGC) target 100%, maximum injection time "auto," and centroid spectrum data type. We use a cycle time of 1 for MS^2 analysis which consisted of HCD high-energy collision dissociation with the following parameters: resolution 50K, AGC 200%, maximum injection time 120ms, isolation window 0.6 Th, normalized collision energy (NCE) 36%, and centroid spectrum data type. Dynamic exclusion was set to automatic. The FAIMS compensation voltages (CV) were −30, −50, and −70V.

Liquid chromatography and tandem mass spectrometry (phosphoproteome)

For phosphopeptide profiling, data were acquired using two injections on an Orbitrap Lumos one with a CV set of −40/-60/-80V and a second injection with a CV set of −30/-40/-50V, both over a 150 min gradient. A 1s TopSpeed cycle was used for each CV. The scan sequence began with an Orbitrap MS1 spectrum with the following parameters: resolution: 60,000, scan range: 350–1350 Th, automatic gain control (AGC): 100%, and maximum injection time: 118 ms. MS2 analysis consisted of higher-energy collisional dissociation (HCD) with the following parameters: resolution: 50,000, AGC: 300%, normalized collision energy (NCE): 36%, maximum injection time: 250 ms, and isolation window: 0.7 Th, and. In addition, unassigned, singly, and >5+ charged species were excluded from MS2 analysis and dynamic exclusion was set to 60 s. The mass spectrometry proteomics data have been deposited to the ProteomeXchange Consortium via the PRIDE[53] partner repository with the dataset identifier PXD051485.

Data analysis

Spectra were converted to mzXML via MSconvert.[61] Database searching included all entries from the human UniProt reference Database (downloaded: August 2021). The database was concatenated with one composed of all protein sequences for that database in reversed order. Searches were performed using a 50-ppm precursor ion tolerance for total protein level profiling and the product ion tolerance was set to 0.03 Da. These wide mass tolerance windows were chosen to maximize sensitivity in conjunction with Comet searches and linear discriminant analysis.[62,63] TMTpro labels on lysine residues and peptide N-termini +304.207 Da), as well as carbamidomethylation of cysteine residues (+57.021 Da) were set as static modifications, while oxidation of methionine residues (+15.995 Da) was set as a variable modification. In addition, deamidation (+0.984 Da) at glutamine and asparagine residues and phosphorylation (+79.966 Da) at serine, threonine, and tyrosine residues were also set as variable modifications for phosphopeptide enrichment. Peptide-spectrum matches (PSMs) were adjusted to a 1% false discovery rate (FDR).[64,65] PSM filtering was performed using a linear discriminant analysis, as described previously[63] and then assembled further to a final

protein-level FDR of 1%.[65] For phosphosite identification, the AScore[62] false-discovery metric was used and only phosphosites that were "high-confidence", with $p \leq 0.05$, were retained. Proteins were quantified by summing reporter ion counts across all matching PSMs, also as described previously.[66] Reporter ion intensities were adjusted to correct for the isotopic impurities of the different TMTpro reagents according to manufacturer specifications. The signal-to-noise measurements of peptides assigned to each protein were summed and these values were normalized so that the sum of the signal for all proteins in each channel was equivalent. Each protein abundance measurement was scaled, such that the summed signal-to-noise for that protein across all channels equals 100.

Quantification and normalization of TMT data

For each plex, first the protein and phosphorylation levels in each channel were re-scaled for protein loading based on the protein levels data. Then, the level of each entry was calculated as the log2 transformation of the ratio to the median value of all TMT channels of that entry (log2 median normalization). Then, every channel was median-centered around zero. Finally, phosphorylation levels were normalized to the total protein levels by subtracting the log-ratio of the corresponding protein from the log-ratio of the phosphorylation site.

Proteomic differential abundance analysis

Differential abundance analysis of proteins and phosphorylation sites was performed using the Limma v3.42 package in R.[67] Because the log-ratio as described above is normally distributed, no voom normalization was applied. Unequal variance between samples was taken into account with the "arrayWeight" function before fitting the model. P-values were computed using a moderated *t* test, and adjusted *p* values (FDR) were calculated using the Benjamini-Hochberg (BH) correction. Significance for differential expression was determined as an FDR ≤ 0.1.

The kinase library analysis

Based on the list of differentially phosphorylated sites described above, kinase enrichment was performed. Full description of the substrate specificities atlas of the Ser/Thr kinome can be found in.[32] The phosphorylation sites detected in this study were scored by all the characterized kinases (303 S/T kinases), and their ranks in the known phosphoproteome score distribution were determined (percentile-score). For every singly phosphorylated site, kinases that ranked within the top-15 kinases for the S/T kinases were considered as biochemically predicted kinases for that phosphorylation site. Toward assessing a kinase motif enrichment, we compared the percentage of phosphorylation sites for which each kinase was predicted among the upregulated and downregulated phosphorylation sites between each two conditions compared (FDR<=0.1), versus the percentage of biochemically favored phosphorylation sites for that kinase within the set of unregulated sites in this study (FDR>0.1). Contingency tables were corrected using Haldane correction. Statistical significance was determined using one-sided Fisher's exact test, and the corresponding *p*-values were adjusted using the Benjamini-Hochberg procedure. Then, for every kinase, the most significant enrichment side (upregulated or downregulated) was selected based on the adjusted *p*-value and presented in the volcano plots and bubblemaps. In the volcano plots, kinases that were significant (adjusted *p*-value ≤ 0.1) for both upregulated and downregulated analysis were plotted on both sides and marked in yellow. Bubble maps were generated with size and color strength representing the adjusted *p*-values and frequency factors respectively, only displaying significant kinases (adjusted *p*-value ≤ 0.1). Kinases that were significant (adjusted *p*-value ≤ 0.1) for both upregulated and downregulated analysis were plotted using the parameters of the more significant side, but were also outlined in yellow.

QUANTIFICATION AND STATISTICAL ANALYSIS

Statistical analyses were performed using GraphPad Prism 9. Two-tailed Student's t-tests were used for single comparison. P-values of <0.05 were considered statistically significant.